Département de Énergétique, thermique et combustion

Numerical modeling of flame acceleration and transition to detonation in narrow channels

Author:
M. Leonardo Nuti 2022269

External-Supervisor:
Dr. Josué Melguizo Gavilanes

Supervisor:
Professor Francesco Barato

Accademic year 2022/2023

Abstract

The capabilities of an OpenFOAM solver recently developed in the detonation Team of l'Institut Pprime were tested to reproduce the behavior of the transition of reactive mixtures to detonation in narrow channels. The process is challenging numerically as it involves the initial ignition of a flame kernel, its subsequent propagation, acceleration, formation of shock waves ahead, and finally detonation onset. Two configurations were considered: (i) channels with wavy walls (10-mm high × 1-m long) that mimic the behavior of fence-type obstacles but prevent abrupt area changes. In this case flame acceleration (FA) is strongly affected by shock-flame interactions, and detonation onset (DO) often results from the compression of the gas present between the accelerating flame front and a converging section of the channel. The effect of increasing the blockage ratio (BR) at constant initial pressure, as well as the effect of initial pressure at constant BR were investigated; the experimentally reported dependence of the run-up distance, x_{DDT}, on the aforementioned parameters is properly captured by our numerical framework. (ii) smooth channels (1-mm high × 1-m long) in which the mechanism responsible for FA is heating due to friction, and in which the effect of flow-induced flame instabilities is suppressed due to the low Reynolds numbers characteristic of this configuration. As a result, the only way of sustaining the increase in burning rate is by the development of "long" finger flames that remain unchanged until DO. Boundary layer heating induced by the flow ahead of the flame makes the flame tip expand towards the walls. Upon contact, a seemingly constant volume explosion takes place that leads to the formation of a cell-less detonation. The effect of resolution on x_{DDT} was assessed; DO occurred further downstream as resolution was increased. The flame morphologies and the DO mechanism, on the other hand, were not found to be affected by resolution. Finally, preliminary tests for a 3-D channel (5-mm × 5-mm cross section; 1-m in length) using Adaptive Mesh Refinement (AMR) are being carried out. Flame inversion and the formation of a tulip flame has been captured so far with the incipient development of asymmetries in one of the flame lobes propagating along the channel's corners. The results so far are encouraging but a detailed analysis of mesh-induced instabilities to the flame morphology needs being done before using AMR confidently.

Contents

List of Figures

Pprime description

Pprime Institute (P') is a research laboratory specialized in the fields of Physics and Engineering Sciences. It is a UPR CNRS linked with the University of Poitiers (The Faculty of Fundamental and Applied Sciences, the Faculty of Sport Sciences, ENSIP (National Higher School of Engineers of Poitiers)) and ISAE-ENSMA (National Higher School of Mechanics and Aeroengineering).

Its research activities cover a large range of topics from physics of materials to fluids and mechanics of materials, mechanical engineering and energetics. It is about using this set of competences, recognized at both national and international levels, to favor collaborations and synergies between different disciplines/subjects, and to respond appropriately the needs of the socioeconomic sector. The privileged areas of application are the transportations and the energy, with a careful consideration given to environmental aspects.

Pprime Institute research activities are developed over 38,000 m^2 of facilities, mainly located at the Futuroscope, but also on the University of Poitiers, Angouleme and Niort universities. The PROMETEE/CEAT technological platform is actually based on Biard and will be established at the Futuroscope at the end of 2016.

Pprime laboratory has been awarded the EQUIPEX programme for its GAP project (Groupe Aéro Propulseur), held by ISAE-ENSMA. It is also a member of the national network of robotics platforms EQUIPEX ROBOTEX held by CNRS and is associated to NANOIMAGESX center (Synchrotron SOLEIL). Pprime controls LABEX INTERACT-IFS, a project held by the University of Poitiers which covers the research programme about fluids and solids interfaces.

Research activities

The department develops fundamental research activities in the field of fluids and energy. It aims to address upstream issues in an original and innovative way in response to problems encountered in the fields of aeronautics and space, land transport, energy and the environment. The main themes addressed concern passenger safety, respect for the environment through performance optimisation and the reduction of polluting emissions and noise pollution in transport.

The "FTC" department thus brings together an important set of skills in complementary disciplines:

- fluid mechanics and aerodynamics, with or without compressibility effects
- heat transfer and associated systems
- premixed or unmixed combustion, possibly heterogeneous, detonation and its applications, (iv) transfer physics and physics applied to electrical phenomena in fluids.

The research carried out within each of the "FTC" axes is based on the development of common methodologies, most often combining the theoretical approach, the development of a wide range of numerical approaches and the implementation of dedicated and consequent experimental installations associated with varied and sophisticated measurement and analysis techniques.

This department is strongly involved in numerous research actions supported by national programmes (ANR, CNRT, GDR), by competitive clusters (Aerospace Valley, Astech, Moveo), by Foundations (FNRAE) and federations (FANO), by the State-Region Project Contract and by the European Community, as well as by all the industrial players.

Introduction

The materialization of a hydrogen economy calls for practical and fundamental understanding of the risks associated with its production, storage and handling. Accidental combustion events include phenomena such as ignition, flame propagation/acceleration, flame-obstacle interactions, shock formation, shock-flame interactions, transition-to-detonation, and detonation propagation. Among these, deflagration-to-detonation transition (DDT) is the most fascinating. From a scientific viewpoint, DDT is an outstanding, physics-rich fundamental problem in combustion. From a practical viewpoint, it is important to understand DDT to develop engineering correlations and simulation tools that can be applied to propulsion, and the prevention/mitigation of explosions. To answer fundamental questions about DDT and examine the details of the process, an in-depth combined experimental, numerical and theoretical effort is needed.

Reacting flows in general, and DDT in particular, are challenging, both experimentally and numerically because of the wide range of spatial and temporal scales at which important physical and chemical processes take place, oftentimes spanning over six orders of magnitude. Conventional methods relying on the discretization of the Reactive Navier-Stokes equations using finite differences/volumes have proven to be effective, and very useful in unveiling the interplay between the chemical heat release and the gas dynamics in high-speed flows. However, their main limitation lies on the fact that the natural path towards tackling larger and more complex, industrially relevant problems is dependent on availability of/access to more computational power (i.e., large computing clusters); specialized mesh treatments such as static/adaptive mesh refinement and recycling meshes are the exception in which the computational power variable is taken as constant and alternatives are sought to do more with less.

This report assesses the capabilities of an OpenFOAM solver [1] recently developed in the detonation Team of l'Institut Pprime to reproduce DDT in partially obstructed and unobstructed narrow channels (i.e., characteristic lengths of the order of mm in which heat and momentum losses to walls are expected to be large) and shows preliminary results on our attempt to implement adaptive mesh refinement (AMR) to the solver. DDT is particularly expensive to compute because the physics at play during each stage of the process changes, and with it, the numerical methods/schemes that would allow for an efficient integration of these type of flows. The initial stages are governed by diffusive processes whereas the latter stages by shock compression. However, the dynamics of flame acceleration (FA) and detonation onset (DO) is highly dependent on the initial acceleration rates that rely on properly capturing the early development of intrinsic flame instabilities, as well as of hydrodynamic boundary layers. Therefore, numerical schemes that perform well for a wide range of Mach numbers are needed. Our solver uses a hybrid implementation for the computation of numerical fluxes. That is, typical pressure-velocity coupling (i.e., Poisson solvers) for low flow velocities ($M \leq 0.3$), and flux-splitting together with appropriate flux limiting (i.e., central-upwind Kurganov-Tadmor scheme [2] with van Albada's limiter) to capture the discontinuities that arise in high-speed flows while avoiding spurious oscillations. The solver is not part of the OpenFOAM standard distribution, and it is based on combining `pisoFoam`, `rhoCentralFoam` and `reactingFoam`.

The ultimate goal, to which the work being done during this internship is contributing, is to develop appropriate tools to reliably simulate the fully optically accessible narrow channel built during the doctoral thesis of Yves Ballossier. So that we can carry out side-by-side comparisons with the experimental data previously/currently being collected. The latter comparison between numerical modeling and experimental data will enable a better understanding of the controlling role exerted by the physical processes occurring at the gas-solid interface (i.e., development of hydrodynamic/thermal boundary layers, species transport, etc.). This report is structured as follows. Chapter 2 briefly describes the physical and numerical methods used. Sections 3.1 and 3.2 describes the domain, initial and boundary conditions used. Sections 3.3 and 3.4 shows results for narrow channels with wavy walls in which the effect of blockage ratio and initial pressure are independently examined. Section 4 includes results for unobstructed channels in which the effect of resolution is discussed; preliminary results with AMR are also included. Finally, concluding remarks and avenues for future work are given in section 5.

Chapter 1

State of the art

The objective of this section is to deepen the review of the current knowledge on DDT in unobstructed and obstructed channels. The work presented in this manuscript is based on publications published between 2008 and 2021. This choice makes it possible to draw up a synthesis of the most recent research published after the literature review by Ciccarelli and Dorofeev [3].

We will use numerical simulations of hydrogen–air in a tube to understand the fundamental mechanisms of deflagration to detonation transition (DDT). We can then apply this understanding to future risk assessment studies for more complex scenarios. Researchers have studied various aspects of flame propagation and the transition from deflagration to detonation in both numerical and experimental studies in an effort to understand the mechanisms associated with DDT [3, 4, 5].

1.0.1 Numerical simulations and theoretical input

In a channel with obstacles, the distance to the DDT is shorter, and thus requires a smaller computational domain, and therefore requires a smaller computational domain. As a result, channels with obstacles are more restrictive in terms of industrial safety. Because of these applied challenges, these channels are the subject of much research. Thus, three-dimensional numerical studies are now common in channels with obstacles [6, 7], sometimes to the detriment of research on unobstructed channels. A better understanding of DDT in channels, which is the central issue of this thesis, is nevertheless crucial on a fundamental level, in order to understand the mechanisms of flame acceleration in a controlled of flames and controlled environment, without the presence of an obstacle. Numerical studies with unobstructed channels examine the DDT in channels of the order of a few square millimetres. This length scale preserves a small computational domain, while capturing the acceleration of the flame as well as the initiation of the detonation. The main results of the numerical studies conducted under these conditions are presented below by author.

Ivanov in [8] first examined 2-D channels, closed on both sides, 5 and 10 mm thick, filled with a stoichiometric mixture of H_2 - O_2. Their results show that the mechanism involved in DDT is the formation of a very high pressure region just in front of the flame. This region favours the propagation of the flame at the local speed of sound. Subsequently, these researchers analysed a channel closed on the ignition side and open on the other side and tested the influence of the height of the D-channel for dimensions of 0.5 mm, 0.8 mm, 1 mm, 2 mm, 3 mm, 5 mm and 10 mm [9]. With a stoichiometric mixture of H_2 - O_2 initially at ambient pressure and temperature, they distinguish a different acceleration dynamic between channels with a height above and below 1 mm. The first phase of exponential acceleration gives way to a phase of deceleration for the larger channels which does not exist in the smaller channels. Using Riemann invariants, these researchers predict the distance between the shock and the flame (5D) and thus the thickness of the laminar boundary layer. Their results highlight that Poiseuil flow is not achieved for channels with > 1 mm before DDT, in contrast to channels with < 1 mm. The deceleration of the flame observed after the initial exponential acceleration phase is therefore due to the coupling between the flow and the flame. Eventually, this coupling tends to enlarge the flame surface but also to cause its inversion ("tulip" flame), temporarily decreasing the flame surface. Their work calls into question the Zel'dovich gradient in the initiation of detonation. As a reminder, the Zel'dovich theory of detonation initiation is based on the formation of the induction time gradient and the one-step Arrhenius chemical model. However, Ivanov compare the Arrhenius model with a model involving detailed chemistry. Their results show that the length of the temperature gradient required to initiate of detonation is one to two orders of magnitude longer than the case with one-step chemistry. The size of a hot spot is therefore too small for the temperature gradient to trigger direct initiation. Their hypothesis is that the cause of detonation initiation lies in the exponential increase of a pressure pulse in front of the flame. However, there is no consensus in the field on these postulates. Indeed, subsequent more detailed research [10, 11] shows that the Zel'dovich gradient is nevertheless responsible for detonation initiation. However, the formation of a hot spot alone is not sufficient and must be accompanied by a significant pressure rise (close to the Von Neumaan state).

Kiverin [12] conducted numerous flame acceleration simulations with a stoichiometric mixture of H_2 - O_2 , in channels with and without obstacles. The unobstructed channel is 5 mm wide and 1 m long, closed on the ignition side and open on the other side. Under these conditions, the researchers examine the structure and stability of the "shocked" flames. To do this, they break down the acceleration of the flame into three stages:

(i) acceleration of the flame to the speed of sound in fresh gas. From this point on, the pressure disturbances are shocked;

(ii) additional acceleration to the speed of sound in the flue gas. At this point, the influence of compression on the chemical kinetics drives the acceleration of the flame;

(iii) potential initiation of detonation.

In the second phase, if the increase in pressure changes the chemical kinetics in such a way that the burning rate increases, there is a transition to detonation. If, on the other hand, it leads to a decrease in the burning rate, a quasi-stationary supersonic flame regime appears. The authors continue the analysis in a more general way in a closed volume [13]. They conclude that the "shocked" regime transits to detonation when the increase in the reaction rate, due to compression, becomes more intense than the increase in the speed of sound in the burnt gases. Their research led to the development of a criterion based on "shocked" flames [14, 15].

Valiev [16] also conducted 2-D numerical simulations in channels that were closed at the ignition and open at the other side. The initial conditions are at ambient pressure and temperature and the fuel used has properties properties of methane and propane. By varying the width of the channel between 0.6 mm to 2 mm, they change the Reynolds number. With a unitary Lewis number, they avoid the number, the researchers avoid the development of thermo-diffusive instabilities. The authors observe several acceleration phases: (i) exponential; (ii) linear increase in velocity (iii) saturation at a deflagration velocity associated with the CJ deflagration velocity [17]. Due to the low Reynolds numbers involved (6.67, 10 and 13.3), the boundary layer does not have time to develop a Poiseuille flow despite the narrowness of the channel. The quasi-stationary propagation mode is further investigated [18]. In order to analyse the effect of hydraulic resistance generating thermal and viscous losses due to the walls, they put forward the work of Brailovsky [19, 20]. The results show that the heating of the reactants by viscous friction becomes important after a first propagation phase. Kagan [21] model the transition from slow flames driven by diffusive effects to a fast flame, accelerated by the compression of the reactants. These researchers show that the asymptotic study of a reduced model correctly captures the thermal runaway caused by the feedback between flame acceleration and preheating by compression and friction. The reduced model employed is only valid for subsonic combustion but can be adapted for supersonic cases. These researchers continue their analysis in [22]. The authors carry out a numerical parametric study based on the model developed by Deshaies and Joulain [23] which takes into account the degree of stretching of the flame. The variation of the tested parameters, the pressure and temperature scaled as well as the degree of stretching, allows the observation of the DDT. The researchers then show the importance of the acceleration of the flame due to the stretching of its surface and/or the proximity of the auto-ignition point in the DDT process.

Akkerman [24] explore the impact of DDT in channels of the order of $0.25 - 1.5$ mm in width. The authors conclude that during the last phase of acceleration, if the reaction time is sufficiently short after the shock, detonation initiation occurs. On the contrary, if the induction length is greater than the flame-shock distance, the flame propagates as a CJ deflagration. Work on millimetre channels and channels with obstacles is summarised in [25]. More recently, Alkhabbaz [26] test the assumption of unit Lewis number in the early stages of acceleration. In the cases of $\mathrm{Le} > 1$, different flame distortion and inversion lead to higher flame acceleration. Furthermore, in cases with $\mathrm{Le} > 1$, an increase in the Reynolds number leads to flame acceleration, whereas it moderates it for a very low Lewis number. This, however, only applies to the first phase of flame acceleration.

Dzieminska [27] focus on the interaction between shocks and the boundary layer in the initiation of detonation. The authors show, in a 2 mm wide channel, that the self-ignition generated in the boundary layer formed by a precursor shock is initiated by the interaction with the following shock wave.

Fukuda [28] pursue this line of research by studying the influence of boundary conditions imposed on the walls (adiabatic or isothermal). Using a 2 mm wide channel, they compare the inclusion of the presence or absence of turbulence in their calculations. The authors note that the self-ignition scenario in the boundary layer is related to the adiabaticity condition on the walls. With an isothermal wall, the flame propagates essentially in the centre of the channel and the initiation of detonation is caused by the interaction of the flame with a curved shock. In contrast, the inclusion of turbulence does cause detonation initiation in the boundary layer, even with isothermal walls.

Machida [29] perform a 3-D simulation of DDT for a stoichiometric mixture in a channel with a cross-section of 1 mm . When an adiabatic condition is imposed on the walls, their results qualitatively reproduce the observations of Urtiew in [30]. A pleated, ogive-shaped flame propagates with its tip located in the centre of the channel. The initiation of detonation then takes place behind the tip of the flame and the shock. The 3-D simulation then locates the explosion coupling the flame and the shock in a corner of the channel.

Melguizo-Gavilanes [31] perform a 3-D simulation in a 100 mm^2 channel. Assuming that the flame propagates symmetrically, the domain size is reduced to one quarter of the channel. The authors observe flame inversion, which persists until the detonation transition. The wall conditions are adiabatic, as in [29], but the difference in cross-sectional size allows the observation of different flame dynamics.

Han [32] corroborate the previous work with a 2-D numerical simulation in channels of

0.22 mm and 12 mm width. In the smaller channel, the authors observe a direct initiation, caused by a bent shock, followed by a velocity deficit of the detonation due to the fluid viscosity. In the largest channel, the transition mode is different. In the early stages of flame propagation, instabilities override the viscosity effect to promote flame acceleration. The role of viscosity is important in the initiation of detonation, compared to its impact in the smaller channel. Indeed, detonation initiation does not take place by direct initiation, but in the near walls, due to the effect of shocked hot spots.

Wang [33] study the impact of channel width (from 5 mm to 20 mm) on the propagation of an ethylene flame using 2-D LES simulations modelling turbulence. They observe a decreasing distance to detonation as the channel width is reduced. Zhao in [34] use the same model to compare the propagation of the methane flame experimentally and numerically in a closed channel of 20 mm width. Under these conditions, the Poiseuille flow is not achieved and the flow remains laminar. The originality of their work lies in the modelling work which, despite a large mesh, reproduces the flame structure before and during the transition.

Huang [35] study the impact of thermal and viscous losses at the walls via 2-D simulations in channels less than a millimetre wide. These losses appear to be more important in small channels. In addition, the heat losses in the boundary layer cause an adverse pressure gradient that leads to oscillatory flame propagation. Numerical simulation work allows to isolate the mechanisms at the centre of flame acceleration and detonation initiation: the compression of the formed shocks, the development of the boundary layer and their influence on the chemical reactions. However, these studies are carried out in 2-D and do not take into account real DDT scenarios. Experimental studies are therefore necessary to verify the validity of these simplified calculations.

1.0.2 Experimental studies

A summary of experimental studies on acceleration and/or DDT in unobstructed channels is given in Tab. 1.1

Xiao [36, 37] investigate the influence of the boundary condition applied at the channel outlet and controlled by the degree of opening. The partially open configuration allows strioscopic observation of the H_2-Air flame acceleration. The degree of openness shows a variety of flame dynamics associated with different modes of flame inversion and distortion. This degree of opening causes variations in the amplitude of the flame position oscillations. By combining experimental studies and numerical simulations [38], these researchers conclude that pressure waves and vortex generation in the flow are involved in the formation of "tulip" flames and their distortion. The paper [39] presents in more detail the early stages of flame propagation in this configuration.

Yu [40] observe the early phases of flame propagation. The authors test five stoichiometric mixtures of H_2-CH_4-Air by varying the proportion of H_2. Using several channels, these researchers also observed the effect of the channel size on the flame inversion. The "tulip" flame is not present in the widest channels, those whose length is too short, or if the proportion of H_2 is too high.

Wu [41] compare the acceleration of an ethylene (C_2H_4) and O_2 flame and its DDT in 0.5 mm, 1 mm and 2 mm diameter tubes. The flame speed increases faster in the 1 mm tubes than in the 2 mm tubes. This is proportional to the ratio of the distance from ignition to the diameter of the tube. In the 0.5 mm tube, detonation is not systematic. Furthermore, the authors observe cases of detonation initiation followed by flame extinction as well as flame propagation at supersonic, quasi-stationary velocity below the CJ detonation velocity. Subsequently, Wu [42] examined the impact of a 3 mm diameter tube and deviated from stoichiometry to extend the experimental range. The authors then map the observed propagation modes as a function of tube diameter and mixture equivalence ratio. As the tube diameter decreases, the range for which DDT is possible becomes narrower. In the case of the 0.5 mm tube, when DDT occurs, a deficit of about 5% of the CJ detonation velocity is reported.

Chan [43] also test the propagation of C_2H_4-O_2 flames in a 1 mm^2 channel. The authors break down the flame acceleration into four stages: (i) first acceleration phase followed by the formation of a precursor shock, (ii) quasi-stationary evolution with an increase in the distance between the shock and the flame, allowing the boundary layer to develop, (iii) second acceleration phase triggered by the stretching of the flame, which is itself caused by the boundary layer, (iv) third acceleration phase with the formation of a shock at the front of the flame that develops into a series of oblique shock waves. The end of the last acceleration phase leads to the initiation of detonation. The development of oblique shock waves is analysed in more detail by Ssu [44]. The angle formed by these shocks depends on both the equivalence ratio of the mixture and the size of the channel. The flame propagates at about 45-50% of the CJ detonation velocity when this group of oblique shocks occurs. The authors show a correlation between the angle of these shocks and the distance to the transition.

Wang[45] use a closed channel of 400 mm^2 to examine, by direct observation, the influence of the proportion of H_2 and the pressure on the DDT. The authors find an increased number of flame oscillations as the H_2 content decreases, an increase in flame speed and a decrease in the distance to the DDT as the pressure increases. They also confirm that the explosive limit of an H_2-O_2 mixture is located between 10% and 90% of the volumetric fraction of H_2 for a pressure between 8 kPa and 60 kPa.

Blanchard [46] investigate the minimum distance to the DDT in a closed channel as a function of the ignition position. Their results show that the position of the ignition influences the reflection of acoustic (or shock) waves on the ends. The distance to the DDT is thus divided by a factor of two if the ignition is not located at one end, or too far from the middle of the channel. Proust [47] compiles his own experiments on flame acceleration in large tubes ($100 - 250$ mm) with those conducted by Kerampran in [48, 49] in small tubes ($22 - 40$ mm). While the flame acceleration and distance to the DDT vary with tube diameter, the influence of mixing is most pronounced. Proust then concludes, in agreement with Keramprans observations, that turbulence plays only a minor role in these configurations.

Thomas [50] address the risk of DDT in linear and curved tubes to be more representative of industrial pipelines. The curvature of the tube is thus of primary importance during the initial phases of acceleration, but its influence decreases as the flame accelerates. The tests conducted with a C_2H_4-Air mixture do not show any sensitivity to the variation of the tube diameter, contrary to the H_2-Air flames, which show that the latter mixture is potentially more sensitive to turbulence. The authors therefore recommend paying particular attention to the ignition conditions of the mixture and the length of the tubes/channels studied. In addition, they point out the limitations of establishing a single criterion for estimating the risks associated with DDT, as it is highly dependent on the geometry, initial conditions and configuration.

Maeda [51] present a study comparing wall roughness in a small channel (12 mm 10 mm). In the case of a rough wall with an arithmetic mean of 100 μm , the flame acceleration is more pronounced. A second flame front forms on the rough walls and results in an inverted funnel-shaped flame.

Aizawa [52] conducted studies of the propagation of premixed and unmixed flames in tubes of various diameters. They control the flow rate of reactants to vary the Reynolds number of the flow and measure its influence on the distance to the DDT. Their results show that the range of equivalence ratios favouring a transition decreases as the tube diameter is reduced. These results are consistent with the observations of [42]. The distances to the DDT are similar to the stoichiometry between the pre-mixed and non-pre-mixed cases. However, this observation is no longer valid when deviating from stoichiometry. Finally, the authors point out that for a low Reynolds value ($Re < 1800$), no influence of the distance to the DDT is visible. If Re becomes larger ($Re = 8800$), the distance to the

DDT decreases by 10%. The increase of the turbulent boundary layer would thus reduce the distance to the DDT, in agreement with the analysis of [53].

Kuznetsov [53] analyse the influence of pressure on the DDT of a H_2-O_2 flame. As a reminder, the authors propose a criterion linking the thickness of the turbulent boundary layer and the size of the cells to evaluate the risk of DDT. Subsequently, these researchers conduct experiments in smaller square channels (50 mm x 50 mm) with different roughnesses [54]. In a channel of this size, the authors observed by strioscopy the formation of a turbulent boundary layer, even in the smooth channel. Kuznetsov and co-workers analyse the length of the preheating zone between the shock and the flame as well as the temperature of this zone, obtained from the shock velocity. Compilation of the results with H_2-O_2 and C_2H_4 mixtures and those obtained by Urtiew and Oppenheim [30], makes it possible to establish a criterion independent of the cell size for anticipating DDT. However, the calculated temperature in the preheating zone does not allow to reach a sufficiently low induction time to cause self-ignition. These results are in agreement with the measurements made by Meyer [55]. Kuznetsov conclude that the preheat zone causes a restructuring of the flame and then the formation of a temperature gradient allowing the formation of a spontaneous wave. The length of the preheat zone favours the propagation of this wave. If the preheat zone is shorter, its temperature must be higher to allow DDT. Liberman [56] compare these experimental results with those from numerical simulations in a narrower channel. They add that the DDT is triggered by a pressure spike generated directly in front of the flame by the formation of a shock in this preheat zone.

Yanez [57] are the only researchers to have published flame spread results of H_2-O_2 and its DDT in a 10 mm, 10 mm, 1000 mm channel, closed at ignition and open on the opposite side. These researchers analyse a particular flame structure but provide only a limited set of data on flame propagation compared to the studies cited above.

Baranyshyn [58] adjust the position of the DDT with the initial pressure in order to examine flame-shock interaction and flame extension. The initiation of detonation occurs mainly between the flame and the shock and sometimes behind the front of the flame. From the data collected, the authors conclude that, in view of the post-shock conditions, the flow must reach an additional $100-200$ K to correspond to the induction time required for DDT initiation. Transverse shock waves, which are not taken into account in the calculation, could be responsible for increasing the temperature by $100-200$ K and reducing the induction time to a value that allows for DDT.

Krivosheyev [59] visualise the propagation of an acetylene (C_2H_2) flame using two cameras positioned at an angle of 90°. This is, to our knowledge, the first simultaneous direct visualisation of flame propagation in an unobstructed tube. Although the authors are not able to visualise the shocks with this method, it nevertheless allows them to reveal the three-dimensional structure of the flame and to confirm that the initiation of the detonation takes place mainly on the wall (86% of the cases). The flame appears very stretched, with a "horn" shape, followed by a "comet tail". This structure then gives way to a variety of initiation modes: (i) spontaneous ignition of two flames and initiation of detonation between these two new secondary flames, (ii) initiation between a secondary flame and the main flame, (iii) initiation in front of a secondary flame, (iv) initiation in front of the main flame (with the absence of a secondary flame)

Source articles	**Mixtures**	**Dimension (mm)**	**Initial Conditions (kPa)**	**Configuration**
Xiao [36, 39]	H_2-Air	$8,2 \times 8,2 \times 530$	$p = 100$	F-O ventilated
Yu [40]	H_2-CH_4-Air	$5 \times 5 \times 25$ to $15 \times 15 \times 100$	$p = 100$	F-O ventilated
Wu [41, 42]	C_2H_4-O_2	$L = 61$; $\phi 0,05/0,1/0,2/0,3$	$p = 100$	O-O
Chan [43]	C_2H_4-O_2	$0,1 \times 0,1 \times 93$	$p = 100$	F-F
Ssu [44]	C_2H_4-O_2	$0,06 \times 0,06 \times 75$ to $0,12 \times 0,12 \times 75$	$p = 100$	F-F
Wang [45]	H_2-O_2	$2 \times 2 \times 150$	$p = 5 - 35$	F-F
Blanchard [46]	H_2-Air	$L = 1800$; $\phi 15,9$	$p = 100$	F-F
Proust [47]	$CnHm/H_2$-Air	$L = 2600$; $\phi 10/25$	$p = 100$	F-O
Thomas [50]	$CnHm/H_2$-Air	$L = 600 - 3000$; $\phi 5/15/30$	$p = 100 - 140$	F-F
Maeda [51]	H_2-O_2	$1,2 \times 1 \times 48,6$	$p = 60 - 100$	F-F
Aizawa [52]	H_2 -Air	$L = 500$; $\phi 2,5/5/10$	$p = 100$	F-O
Kuznetsov [53]	H_2-O_2	$L = 2500$; $\phi 10,5$	$p = 20 - 800$	F-F
Kuznetsov [60, 54]	C_2H_4/H_2-O_2	$5 \times 5 \times 340/606,5$	$p = 20 - 75$	F-F
Yanez [57]	H_2-O_2	$0,5 \times 0,5 \times 100 and 1 \times 1 \times 100$	$p = 100$	F-O
Baranyshyn [58]	C_2H_2-O_2-Ar/N_2	$L = 664$; $\phi 4$	$p = 13,6 - 50$	F-F
Krivosheyev [59]	C_2H_2-O_2-Ar/N_2	$L = 600$; $\phi 6/9$	$p = 16 - 17,5$	F-F

Table 1.1: Parameters for experimental studies of flame acceleration and detonation initiation in unimpeded channels. Dimensions in width (W) × height (H) × length (L) format, or length and diameter. F-O closed at the ignition side - open at the exit; F-F closed on both sides. These studies are performed at room temperature.

Experimental studies of flame propagation in unobstructed channels cover a wide range of dimensions, configurations and mixtures. Several key issues in the DDT phenomenon remain to be elucidated. In particular, what characteristic length to use to determine the Reynolds number of the flame (height, diameter, thickness of the flame, etc.)? From what Reynolds number and what shock-flame distance can the boundary layer be considered as turbulent? What are the main mechanisms responsible for the temperature rise between the flame and the shock? Is the temperature rise mainly due to pre-compression by the precursor shock, viscous friction in the boundary layer, reflections from transverse shocks? Is the Zeld'ovich gradient always the cause of DDT initiation? Are these direct ignitions behind a strong shock? In order to contribute to the answers to these questions and to understand the fundamental aspects of DDT, experimental studies in an unobstructed channel are still needed.

1.0.3 Obstacles configurations

We were particularly interested in configurations involving obstacles, and were performing numerical simulations, so we generally focused on numerical studies of DDT involving obstacles. Many of the studies on DDT have considered obstructed flows because literature has shown [61, 62, 63] that the addition of obstacles reduces the time and distance to a potential detonation, making it easier to run experiments and numerical simulations that capture DDT.

Gaathaug [64] showed that even one obstacle in the flow can result in transition to detonation. With the addition of obstacles, a number of additional parameters are variable such as size, shape, and placement of obstacles. Teodorczyk [61] conducted experiments with rectangular obstacles in a hydrogen–air environment to determine regimes for deflagrations, transition, and detonations. The results showed that increasing the blockage ratio decreased the DDT hazard, while increasing the spacing between obstacles with high blockage ratios increased the DDT hazard. These accelerated flames drive pressure waves with large overpressures, a concern in the present work for risk analyses, and can then transition to detonation.

Also the review of Strebel [65] faces many different types of geometries that have been used in heat exchangers and subsequently studied numerically and experimentally. For this thesis the serpentine wavy channel is used, but a review of all types of geometries is used to minimize the soot deposition. A fully implicit BFC code was developed to solve the Navier-Stokes equations in conjunction with the energy and concentration equations. The friction factor times the Reynolds number was shown to oscillate periodically due to the wavy geometry, with peaks in the values occurring every time the flow was required to change direction. Overall the pressure drop was shown to increase with increasing wall temperature and decrease with increasing wall temperature. Compared to the planar channel the pressure drop was larger, as expected. The Nusselt number was also shown to oscillate, and increase with both increasing Reynolds number and increasing temperature gradient. Again, the overall heat transfer was larger for a wavy channel than for a planar channel. Finally the deposition efficiency was shown to increase with temperature gradient and decrease with Reynolds number. But the decrease with Reynolds number is likely due to the lower fluid residence time for larger Reynolds numbers. The comparison between wavy and planar channels showed that the wavy geometry does cause the deposition to increase.

Zakaria [66], in this work, an innovative MC configuration with wavy walls for thermo-photovoltaic applications it has been proposed. The innovative wavy walls could contain 2-waves, 4-waves or 8-waves. The wavy walls ensure an enhanced heat transfer between the reactor and the absorber of the MTPV system. Within the proposed MC configuration the micro-combustion characteristics of 2D laminar premixed CH_4–air flames ($\phi = 1$) have been studied numerically.

Reza Soleimanpour and Hossain Nemati [67] faced with the DDT of H_2–O_2 in some closed ducts that have been investigated using OpenFOAM package and the results have been compared with experimental data. It has been seen doubling the amplitude changes of the wall, the flame progresses with a highly different approach and the speed of the flame tip is much higher. In the second geometry, according to the considered amplitude, the sinusoidal wall again increases the turbulence intensity as well as the reaction rate, and all of this help to accelerate the DDT phenomenon.

Based on the studies mentioned above, we focused on a channel with smooth obstacles; a symmetrical corrugated channel to study its pressure wave reflection characteristics and its effects on detonation initiation and flame morphology. We then move on to an unobstructed channel to numerically analyse the evolution of the flame and the effects of the boundary layer. These analyses were carried out by testing our solver on OpenFOAM, which is capable of analysing the evolutionary characteristics of reactive flows and their chemical kinetics using an H_2-Air mixture. Different types of channel obstruction ratios and the comparison of different initial pressures were also compared, analyses that have not yet been covered by the mentioned studies. These results can be compared with the experiments that have already been done, and as far as the unobstructed channel is concerned, it can also be compared with the practical experiments that we are carrying out in the Pprime laboratories, with the same channel dimensions, conducted by PhD student Cristian Camilo Mejia Botero under the supervision of our supervisor Dr. Josué Melguizo-Gavilanes in the Fluides, Thermique and Combustion department.

Chapter 2

Physical Model

2.1 Governing equations

The flow field in the channel was modeled using the reactive Navier Stokes equations with detailed chemistry and temperature dependent transport and thermodynamics (i.e., JANAF tables to compute species/mixture heat capacities, enthalpies and entropies) [68]. The Sutherland Law [69], modified Eucken relation [70] and JANAF polynomials [68] are used to account for the functional temperature dependence of mixture viscosity (μ), thermal conductivity (κ) and specific heat (c_p), respectively.

$$\partial_t \rho + \nabla \cdot (\rho \mathbf{u}) = 0 \quad \text{(Mass)} \tag{2.1}$$

$$\partial_t (\rho \mathbf{u}) + \nabla \cdot (\rho \mathbf{u}\mathbf{u}) = -\nabla p + \nabla \cdot \tau \quad \text{(Momentum)} \tag{2.2}$$

$$\partial_t (\rho Y_k) + \nabla \cdot (\rho \mathbf{u} Y_k) = -\nabla \cdot \mathbf{j_k} + \dot{\omega}_k \quad \text{(Species)} \tag{2.3}$$

$$\partial_t [\rho (h_s + K)] + \nabla \cdot [\rho \mathbf{u} (h_s + K)] = \frac{dp}{dt} - \nabla \cdot \mathbf{j_q} + \tau : \nabla \mathbf{u} + \dot{q}_{\text{chem}} \quad \text{(Energy)} \tag{2.4}$$

$$p = \rho \frac{R_u}{W_{\text{mix}}} T \tag{2.5}$$

with $K = \frac{1}{2}|\mathbf{u}|^2$; $\tau = \mu(\nabla \mathbf{u} + \nabla \mathbf{u}^T) - \frac{2}{3}\mu(\nabla \cdot \mathbf{u})\mathbf{I}$; $\dot{q}_{\text{chem}} = \sum_{k=1}^{N} \Delta h^0_{f,i} \dot{\omega}_k$

Where ρ is the density, $\mathbf{u}$ is the velocity, p is the pressure, h is the sensible enthalpy per unit volume, Y is the mass fraction of the k-th species, $\dot{\omega}_k$ is the reaction rate for the k-th species . With a number of equations which increase as much as there are species, with τ, viscous stress tensor, $\mathbf{j_k}$ is the species diffusion flux, $\mathbf{j_q}$ is the heat flux, $\dot{q}_{\text{chem}}$ is the rate of conversion of chemical into thermal energy, $\Delta h^0_{f,i}$ is the enthalpy of formation of species, R_u is the specific gas constant, μ is the mixture viscosity. The species diffusion term, $\mathbf{j_k}$, uses Fick's law for binary mixtures. For multicomponent mixtures where one component is present in large amounts (i.e., N_2 for combustion in air) all other species may be treated as trace species. Writing the binary diffusion coefficient with respect to N_2 only yields:

$$\mathbf{j_k} = -\rho D_k \nabla Y_k \tag{2.6}$$

where D_k is the effective diffusion coefficient. In Eq. 2.6, thermodiffusion or Soret effect has been neglected. We solve the mass conservation equation, Eq. 2.3, and only for $N-1$ species equations. The last species mass fraction, N_2 , is obtained by writing $Y_{N_2} = 1 - \sum_{k=1}^{N-1} Y_k$ and absorbs all inconsistencies introduced by Fick's law. This error is negligible when the last species, Y_{N_2} , is at a high concentration as is the case for combustion in air [71]. The heat flux $\mathbf{j_q}$ includes the effect of sensible enthalpy transport by diffusion

$$\mathbf{j_q} = -\frac{\kappa}{c_p}\nabla h_s + \sum_{k=1}^{N-1} h_{s,k}\left(\mathbf{j_k} - \frac{\kappa}{c_p}\nabla Y_k\right) \tag{2.7}$$

In Eq. 2.7, the Dufour effect (i.e., energy flux due to a concentration gradient) has not been taken into account [72]. Substituting Eq. 2.6 into 2.7 yields:

$$\mathbf{j_q} = -\frac{\kappa}{c_p}\nabla h_s + \sum_{k=1}^{N-1} h_{s,k}\left(1 - \frac{1}{Le_k}\right)\frac{\kappa}{c_p}\nabla Y_k \tag{2.8}$$

where $Le_k = \kappa/(c_p \rho D_k)$ is the Lewis number of species k. The Lewis number is assumed to be unity for all species which results in $\kappa/c_p = \rho D_k$. Hence, the dynamic thermal diffusivity of species is used to model its mass diffusivity. The second term on the right hand side of Eq. 2.8 vanishes if the Lewis numbers of all species are assumed to be unity, simplifying the energy equation significantly. The governing equations were solved in a two-dimensional planar geometry using the OpenFOAM Toolbox [1]; chemical kinetics was modeled with the 9-species, 21- reactions Mével's mechanism for hydrogen-oxidation [73], whose ignition delay time predictions (metric of in-terest in the current study) are neither the fastest nor the slowest among the available alternatives. The spatial discretization of the solution domain is performed using finite volumes (FV) which allows for body-fitted 6hexagonal meshes that avoid the staircasing present when numerically integrating curved geometries with finite differences. The solver includes a hybrid implementation for the numerical fluxes that make it suitable for a wide range of Mach numbers; this is achieved by combining PISO methods (i.e., pressure-velocity coupling) in regions with low flow velocities ($M \leq 0.3$), together with standard techniques for high speed flows (i.e. flux-splitting and limiters). The numerical fluxes at cell-faces are thus computed using a central-upwind Kurganov-Tadmor scheme [2]. The flow variables on cell faces are reconstructed through a second-order interpolation with a symmetric van Albada flux limiter which results in non-oscillatory bounded transitions across shocks and contact discontinuities. The chemical source terms are computed using a stiff ODE solver (i.e., fourth order Rosenbrock). The PBiCGStab (Preconditioned Biconjugate Gradient Stabilized) method is used for all the linear systems resulting from the discretization of the governing equations, preconditioned through the DILU (Diagonal Incomplete-LU) technique. Finally, the time integration uses a second order Crank-Nicolson method, and the time step is dynamically adapted during the computation with an acoustic Courant number of 0.4 to ensure stability of the numerical scheme.

Chapter 3

Obstructed channels

3.1 Domain, initial and boundary conditions

First of all, the domain of our interest was created, via a C++ script within the blockMesh dictionary. It has permitted us to recreate the geometry of a wavy channel and using some geometry parameters to change it and analyze more wide cases of study.

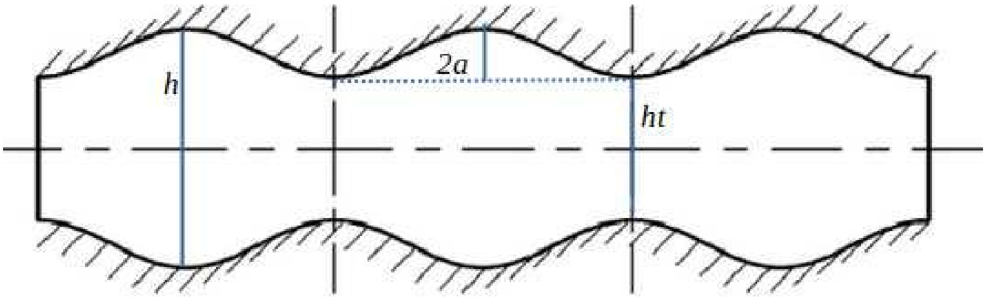

Figure 3.1: Physical domain and geometrical parameters used to define it.

Geometry parameters:

- $h = 10$; channel height in mm
- $L = 1000$; channel length in mm
- $\delta = 0.38$; flame thickness in mm
- Npts/$\delta = 3$; number of points per flame thickness
- $z = 1$; depth of channel in mm

- $a = 0.1$; amplitude of wave percentage of height of channel [0,1]
- $b = 1.25$; wavelength; multiple of flame thickness delta
- $c = 0.5$; offset of sine wave top wall; multiple of flame thickness delta
- $c_1 = 0.0$; offset of sine wave bottom wall; multiple of flame thickness δ

$$y_{\text{top}} = ah \sin\left(\frac{x - cb\delta}{b\delta} 2\pi\right) + h(1-a) \tag{3.1}$$

$$y_{\text{bottom}} = ah \sin\left(\frac{x}{b\delta} 2\pi\right) + ah \tag{3.2}$$

The simulation has been carried in 2D. The number of cells in each direction is 7894 in x-direction, 78 in y-direction, 1 in z-direction, for a total of 615732 of cells for the entire domain and with uniform expansions in the local x, y, z (simpleGrading (1 1 1)). This corresponds to an approximately uniform mesh along the length and height of the channel of $\Delta x = \Delta y = 0.128$ mm. The a parameter, amplitude of wave percentage of height of channel is represented as follows.

And the blockage ratio (BR) is computed as follows:

$$BR = \frac{h - ht}{h} = 1 - \frac{h - 4a}{h} \tag{3.3}$$

With a expressed as function of the height of the channel (i.e., $a = xh$), where $x = [0, 1]$.

Modifying with the 'a' parameter we are able to modify the blockage ratio (BR) of our channel and investigate on additional cases.

Three blockage ratios are considered:

- $BR = 0.2$; $a = 0.05h$
- $BR = 0.4$; $a = 0.1h$
- $BR = 0.6$; $a = 0.15h$

3.2 Initial and boundary conditions

Three initial pressures were considered $p_0 = 25$, 50, 100 kPa to investigate the FA dynamics in the channel for $BR = 0.6$, when investigating the effect of BR on the aforementioned dynamics one initial pressure was fixed to 100 kPa. The channel was filled with quiescent

Combustion properties	$p_0 = 25$ kPa	$p_0 = 50$ kPa	$p_0 = 100$ kPa
Laminar burning velocity, s_L	2.18 m/s	2.32 m/s	2.38 m/s
Expansion ratio, σ	6.71	6.77	6.81
Flame thickness, δ	2.31 mm	0.91 mm	0.36 mm
Burnt products sound speed, c_b	999.34 m/s	1002.93 m/s	1005.8 m/s
CJ speed, D_{CJ}	1936.93 m/s	1952.82 m/s	1967.84 m/s
Induction length, l_{ind}	0.56 mm	0.27 mm	0.14 mm

Table 3.1: Combustion properties for stocihiometric H_2-air at different initial pressures and $T_0 = 300$ K.

mixture at $T_0 = 300$ K, and mass fractions $Y_{H_2} = 0.02851$, $Y_{O_2} = 0.22628$, $Y_{N_2} = 0.74521$, corresponding to a stoichiometric H_2-air mixture in all cases, and the chemistry was modeled using the detailed mechanism of Mével that includes 9 species H_2, O_2, O, H_2O, H, OH, HO_2, H_2O_2, N_2, and 21 reactions. No turbulence models are used. Regarding boundary conditions, the channels are closed at the ignition end and open on the other end; zero gradient for all scalars, i.e., (p, T, Y_k), and no-slip for velocity on the channel's walls. Given the chosen mesh size, there are $\sim$ 18 pts, 7 pts, 3 pts, per flame thickness for 25 kPa, 50 kPa and 100 kPa, respectively. In terms of the detonation induction length there are 5 pts, 2 pts and 1 pts as the initial pressure increases. Finally, the flame was ignited by imposing three equally spaced hemi-spherical regions ($r = 1.2$ mm) of high pressure ($p_{\text{ign}}/p_0 = 5$) and temperature ($T_{\text{ign}}/T_0 = 6.6$) at the channel closed end, as shown in Fig. 3.2.

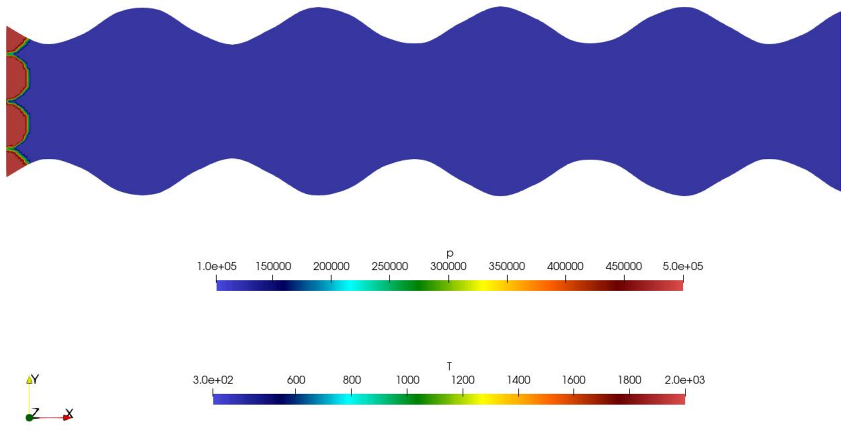

Figure 3.2: Set field ignition, p (Pa) and T (K), ($BR = 0.4$).

3.3 Effects of BR at fixed initial pressure

Several cases were tried out to test the reliability and concreteness of the OpenFOAM software in a 2D case. The results of these cases are divided according to the channel's blockage ratio (BR) and according to the setting of the initial ignition conditions. The numerically predicted and experimentally observed dynamics of the detonation as it propagated through the wavy channel is shown below as graphically represented through space-time diagrams, post-processed after completing the simulations, comparing the cases of fixed initial pressure and change in blockage ratio vs. fixed blockage ratio and change in initial ignition pressure. The trend of flames topology is presented in the subsection from 3.3.2 to 3.3.5.

3.3.1 Overall dynamics

By simulating through our numerical model, the dynamic trend of the evolution of the flame inside the channel and post-processing the acquired data, we were able to recreate an evolutionary trend showing the differences in the attainment of the detonation state between different cases of BR at fixed pressure in the first graph, fig. 3.3 and 3.4. (For fig. 3.4, $BR = 0.2$ we missed some data after DDT onset as we stopped the simulation shortly after obtaining the detonation regime.)

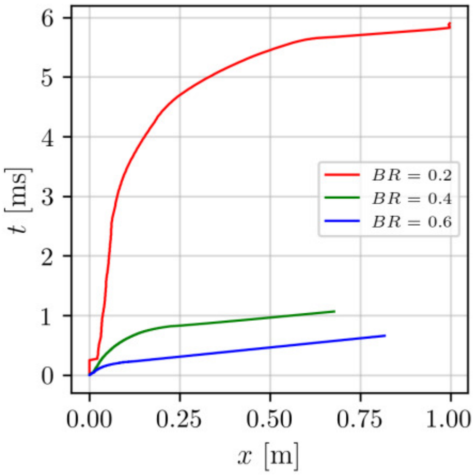

Figure 3.3: $x - t$ diagram at different BR

In addition, studies by Lindsted and Michels [74] and Kuznestov et al. [3, 60, 53, 75], concerning the run-up distance, i.e., the necessary distance the flame must reach in order to transition into detonation using a simple analytical model, were presented, equation 3.4. This experimental mathematical model, used for a straight flow in the presence of a boundary layer, shows where the flame practically reaches the speed of sound in the

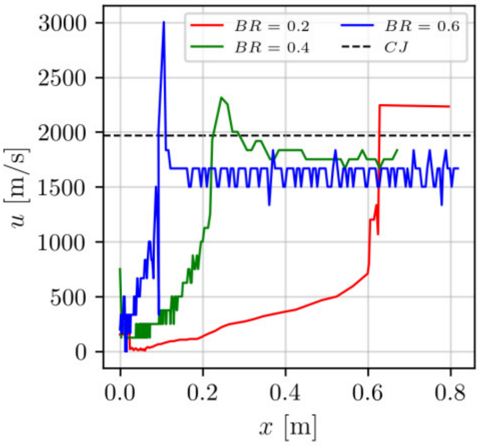

Figure 3.4: $u - x$ diagram at different BR

BR	$x_{\mathbf{DDT}}$ (m)	Evolution %	$x = x_{\mathbf{DDT}}0.5$ (m)
0.6	0.09	50	0.05
0.4	0.21	50	0.11
0.2	0.62	50	0.31

Table 3.2: X evolution flame distances at fixed $p_0 = 100$ kPa

products of combustion before detonation occurs, using a simple equation as a function of tube diameter. The model has a prediction accuracy in the range of ±25%. Using such a model for our case we find a deviation of about 40, 50%, probably due to having a corrugated channel, furthermore the run-up distance is closely related to the BR of the channel and the mixture used.

$$\frac{x_{\mathrm{DDT}}}{D} = \frac{\gamma}{C}\left[\frac{1}{\kappa}\ln\left(\gamma\frac{D}{h}\right) + K\right] \tag{3.4}$$

$$\gamma = \left[\frac{a_p}{\eta(\sigma-1)^2 S_l}\frac{\delta}{D}^{\left(\frac{1}{3}\right)}\right]^{\left(\frac{1}{2m+\frac{7}{3}}\right)} \tag{3.5}$$

Dealing with flame evolution that change depending on the boundary conditions is not useful to compare them in the same simulation time or at the same channel distance. Therefore, the evolution distances for comparison were normalized to the distance reached by the first DDT phase (x_{DDT}), (see fig. 3.5) even if the detonation regime does not then set up correctly, see example below, in the tables 3.2. In such a way as to compare approximately the same evolutionary state for each difference in BR.

The evolution of flame acceleration is subdivided as follows:

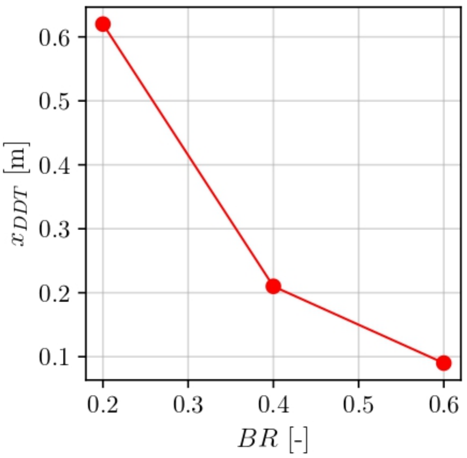

Figure 3.5: x_{DDT} vs. differents BRs

- Early stages: likely between 10-50
- Intermediate stages: 50-70%
- Late stages: 70-90%
- Moments prior to DDT: 90-98%
- >100%: Detonation propagation

3.3.2 Early and intermediate stages of flame acceleration

We focused on the differences in flame topology as the blockage ratio changes while keeping the initial conditions unchanged, of $p_0 = 100$ kPa and $T_0 = 300$K. Making the simulation go, the flame starts to propagate through the channel, generating an initial shock wave, which begins to propagate through the channel, driven by the chemical combustion process and the dimensional parameters of the channel, with a maximum height of 10 mm and a total length of 1 m, as seen in fig. 3.6. Likewise, the flame speed and temperature increase upon entering the flame acceleration regime, the deflagration propagates through the mixture of fuel and oxidizer in a subsonic combustion, thermal expansion of the combustion products produces movement in the unburned gas. The flow interaction with the boundaries causes an increase of the flame surface; and this results in an increase of flame speed and flow velocity relative to a fixed observer. The pressure in turn begins to increase at the converging and diverging edges of the channel due to the formation of shock waves at the flame front. Although deflagration occurs throughout the channel, recirculation zones form along the edges of the diverging zones, leaving behind pockets of fresh, unburnt mixture, behind the flame. The phenomenon occurs due to the fact that the undulating domain of the channel slices the flame surface, resulting in an increase in flow velocity during the compression in the converging part. The sudden onset of accelerated flow in the expansion of a diverging part produces a pair of laminar vortices on the downstream edge after each throat. These eddies grow in a recirculation pocket that occupy a part of the inner volume of the duct. At the same time, a shear layer develops separating the recirculation zones and the core flow, and if the flame reaches a vortex after the shear layer has developed the flame propagate in the core flow and only after, burns into the pocket's regions. This leads to the development of intense recirculation within the flow. This turbulence increases the combustion ratio, the surface area of the flame and the transport of mass and energy, causing the flow to approach high and near transonic velocities. The flame morphologies for the various BRs at $x = 0.65 x_{\mathrm{DDT}}$ are shown in figs.3.7 .

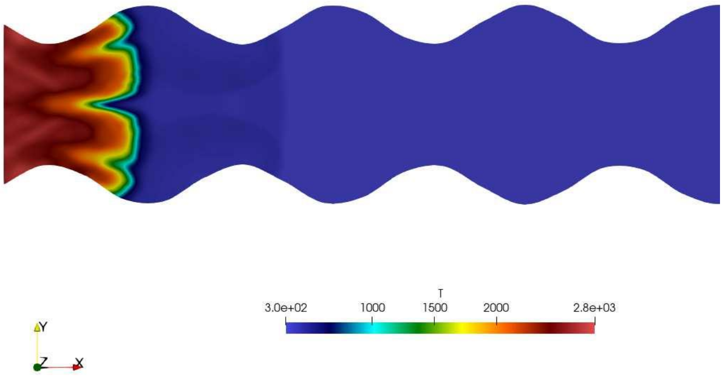

Figure 3.6: Initial flame propagation and downstream shock wave generation ($BR = 0.6$), early stage 10%

As can be seen from the pictures, the recirculation zones are more pronounced, moving from small BR towards larger BR. In figure 3.7(c), the recirculation pockets of unburned gas are much more defined, and this behavior due to the amplitude of the convergent-divergent sections can lead to the formation of critical zones of high pressure, density and temperature as the flame velocity increases and the flame surface increases due to interaction with shock waves, which impact a larger blockage along the channel, shown in a Schlieren fig. 3.8.This behavior is the same as that described for obstructed channels, using fenced type obstacles presented in the review by G. Ciccarelli and S. Dorofeev [3].

3.3.3 Moments prior to DDT

The detonation initiation is the result of flame acceleration, the flame run-up distance, x_{DDT}, is considered a property of the mixture, the domain and in our case also of the

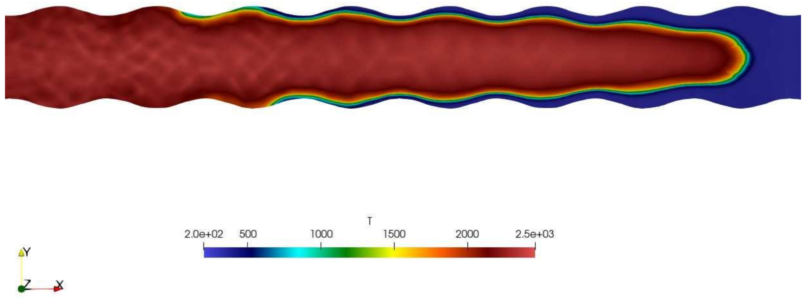

a) $BR = 0.2$

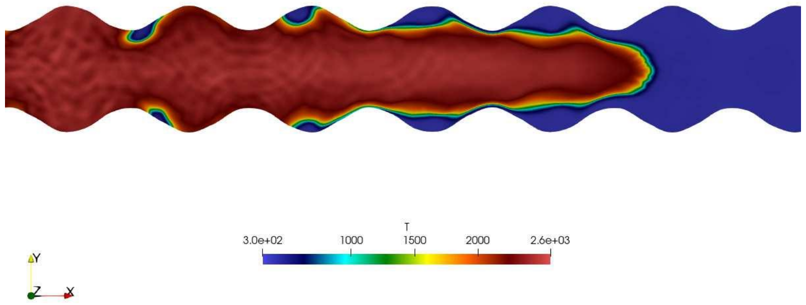

b) $BR = 0.4$

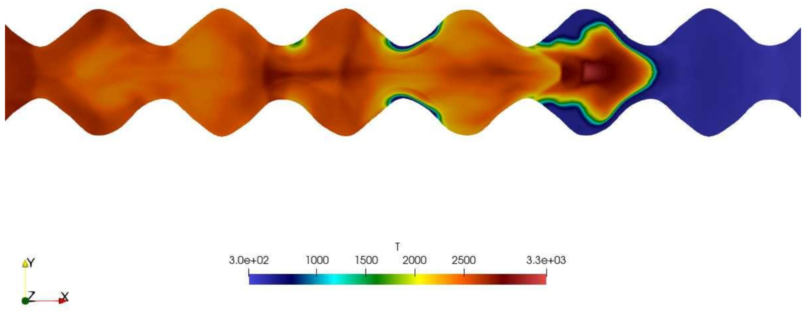

c) $BR = 0.6$

Figure 3.7: Recirculation zones for each blockage ratio at 65% (intermediate stage) of the evolution flame from the beginning of the channel.

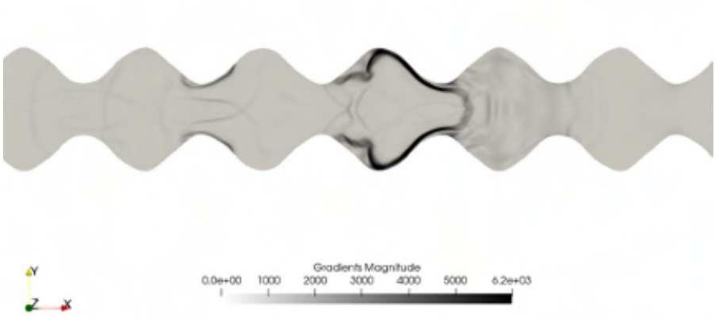

Figure 3.8: Schlieren picture of recirculating zones (rho density) $BR = 0.2$

mesh resolution. Several past papers dealing with flame acceleration in tubes, see [3], have described the transition process as a phenomenon requiring: 1) that the flame should reach a sufficiently high velocity for detonation to occur, at least of the order of the speed of sound of the combustion products. 2) The opening of the obstructed channel must be sufficiently wide, at least of the order of the detonation cell width of the mixture in tube. In sufficiently long channels the velocity profile is expected, at some stage, a shock wave coalesce is generated in front of the flame front, as is shown in fig. 3.9, and the behavior is the same for each BRs. The shock waves formed at the flame front are reflected on the edges of the channel, bouncing from one wall to the other and also propagating in the opposite direction to the flame motion. The thermal expansion of the combustion products generates motion in the unburned gases, this leads to the formation of strong movements and temperature and pressure increases at the most critical points. Pressure waves, which propagates at the local speed of sound, coalescence, generating shock waves and impacting the edges of the converging channel, creating areas of very high density and pressure that could trigger the detonation phenomenon. In our case it is the interactions of the flame with the boundaries and shock waves that result in a significant increase of the burning rate near the channel's walls. A few moments before the detonation regime sets in, when the flame reaches considerable velocity, it gets closer and closer to the shock waves created at the flame front. This characteristic causes the induction zone, shown in the following images of the channel fig. 3.10, characterized by the green band, the reaction zone represented by the orange band and the combustion gas zone, represented by the red band behind the flame, to become increasingly thinner, leading to an extremely critical condition. The closer we approach the velocities of the shock waves in front of the flame, the more these bands flatten out, thus shortening the time and space required for the reactions to take place. In particular, reactions take place in the orange band around the surface of the flame, and it can be seen that in an intermediate state of flame evolution, the orange band is more spread out and affects much more of the surface of the flame. This state is also characterized by a 'finger' shape of the flame, after which the accelerating flame changes shape due to the increasingly intense instabilities generated, which leads to a reduction of the flame surface where reactions can take place, and to a flattening of the reaction zone.

3.3.4 Onset of detonation

The conditions necessary for the onset of detonation is the localized formation of small explosions occurring somewhere in the fresh mixture subjected to critical conditions of high pressure, density and temperature. Generally, such conditions are generated by strong compressions and/or turbulent mixing of products and reactants, and the process can be triggered in a wide variety of situations. According to past experience, the occurrence of detonation can be classified into two categories: 1) Onset of detonation arising from reflection of shock waves in coalescing shockwave packing zones. 2) Onset of detonation caused by instabilities, discontinuities and particular mixing processes in the mixture:

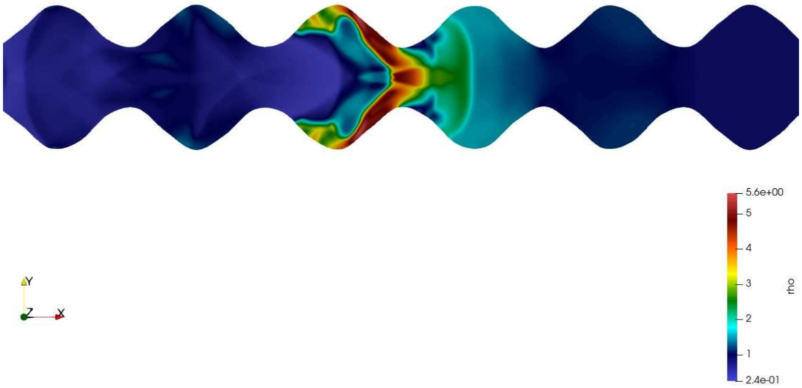

a) $BR = 0.6$

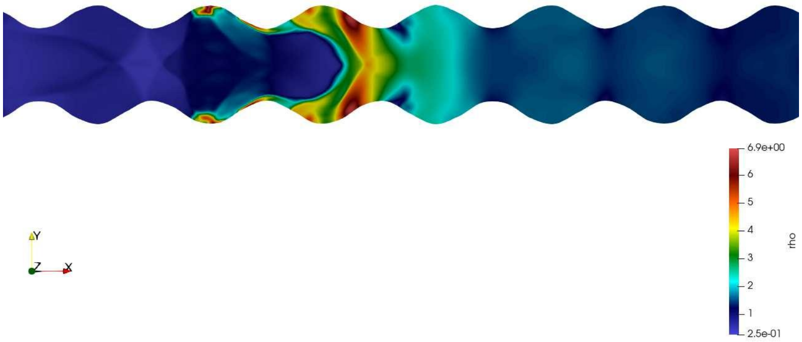

b) $BR = 0.4$

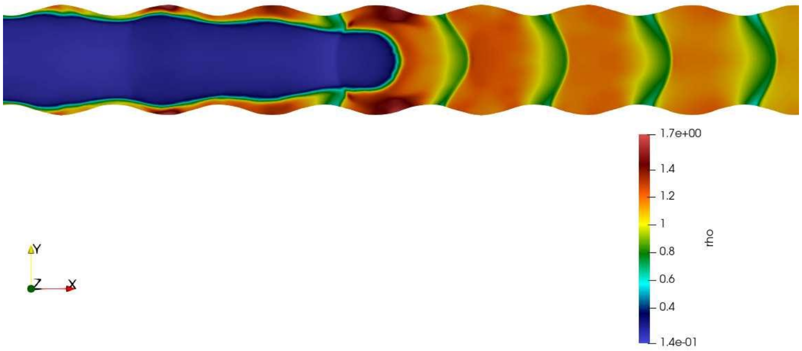

c) $BR = 0.2$

Figure 3.9: Shock wave ahead at 90% of the evolution: a) $BR = 0.6$; b) $BR = 0.4$; c) $BR = 0.2$

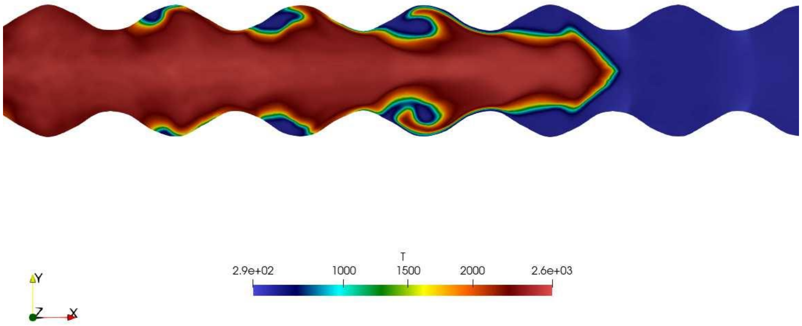

a) $x \sim 0.7 x_{\mathrm{DDT}}$

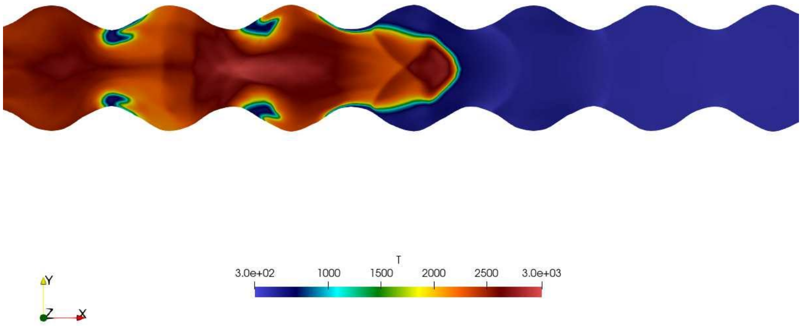

b) $x \sim 0.85 x_{\mathrm{DDT}}$

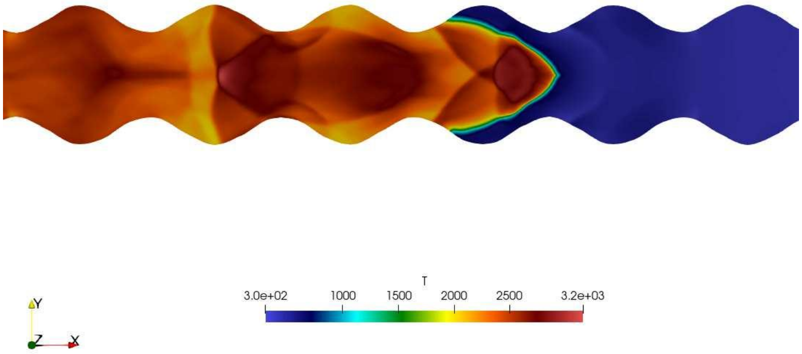

c) $x \sim 0.95 x_{\mathrm{DDT}}$

Figure 3.10: Induction, reaction zones of the flame at different stages of the evolution at $BR = 0.4$ a) 70% intermediate stage of the flame; b) 85% late stage of the flame; c) 95% moments prior ddt

- instability near the flame front;
- Flow interactions with pressure waves and contours or obstacles along the way;
- Eventual explosion of quenched pockets of fresh mixture behind the flame front, (which can accelerate the flame further);
- Pressure and fluctuations in the flow and boundary layer.

In sufficiently long channels typically a fuel-air mixture can reach speeds in the order of 600 − 1000 m/s. The transition to detonation can be observed when the flame reaches speeds on the order of the speed of sound of the products of combustion. For these cases, with this mixture composition and initial conditions, the calculated speed of sound in the products of combustion is approximately 1000 m/s; see table 3.1 for exact number.

In our case, we observe a combination of the two categories of DDT onset. The shock waves generated ahead of the flame that result from the strong acceleration of the flame itself, which is drawn in and propelled by a complex system of reflection of shock waves and probably small explosions due to the critical points created in the impact between the shock waves themselves, producing shock focusing, as depicted in the fig. **??** of $BR = 0.4$ channel.

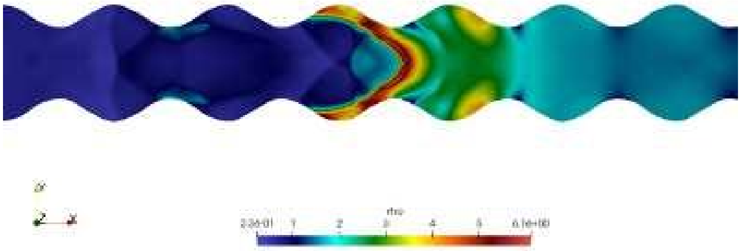

Figure 3.11: Flame propelled by shock waves ahead, 95% of evolution, $BR = 0.4$

3.3.5 Detonation propagation

It can be seen how the shock waves formed in front of the flame front interact with the edges of the converging channel, probably arising in small explosions and in turn generating a pair of reflection waves, which propagate towards the centre of the channel, impacting more or less at the centre of the domain and generating a critical point which may be subject to detonation. These explosions generate pressure waves that propagate both along the flame direction and in the opposite direction, creating the conditions for a possible transition to detonation. This process is repeated for each converging diverging channel section with increasingly critical conditions, until the flame front is pushed sufficiently beyond the shock waves, then the onset of detonation sets in, and the flow attempts to sustain this regime. Before the detonation has occurred, depending on the properties of the mixture, boundary conditions, the interaction of the flame with the flow in the unburned gas, the roughness (inexperiments) of the channel or the shape of the domain, in simulations leads to an energy release rate that is high enough to result in supersonic combustion, which may reach:

- A steady state detonation;
- Quenching;
- Choking;
- Quasi-detonation regime.

The later stages of the process, namely the propagation of detonation for cases with different BR is shown below through numerical soot foils, which represent the trajectory of triple points in the domain, fig 3.12.

In our cases, the reaction front reaches a steady state of propagation with speeds of 1000 m/s, for $BR = 0.2$ and $BR = 0.4$. As for the case with $BR = 0.6$, the detonation regime never settles completely; subsequent reinitiation and failures result in the development of a quasi-detonation regime. An actual indication of this type of regime is given by the numerical soot foil, fig. 3.12(c), where the characteristic cellular structure of detonations (which will be explained below) is not as well defined and clear as in the other two cases. Fig. 3.12(a,b). As illustrated in the picture, the reaction front has reached a steady state and reappears with the same characteristics for each section in front of it, until the end of the channel. The reflection of the shock waves in front of and behind the flame continue to propel it at high speed and chemical reaction takes place at the head of the detonation wave where a shock wave is followed by a thin reaction zone, fig. 3.13

We can also observe the formation of the characteristic cellular structure of detonations, as depicted in the soot foils images fig. 3.14, where the triple points [76] are formed by the intersection of the detonation wave, oblique shock wave and Prandtl Meyer expansion waves. Experiments have demonstrated that most self-sustaining detonations are intrinsically unstable, the lead shock consists of weak incident wave and stronger Mach stem intersect at triple point with the transverse waves, which sweep laterally across the leading shock and collide with each other. The leading wrinkled shock consists of alternate weak incident shocks, stronger Mach stems and transverse waves that interact at the so-called triple points.

Although detonation fronts appear remarkably flat in images, the flow is clearly non-uniform behind the front with a series of periodic streaks extending horizontally to the rear of the main flow. Although these transverse waves appear to be weak perturbations on a predominantly one-dimensional flow, they can have a profound effect on the behavior

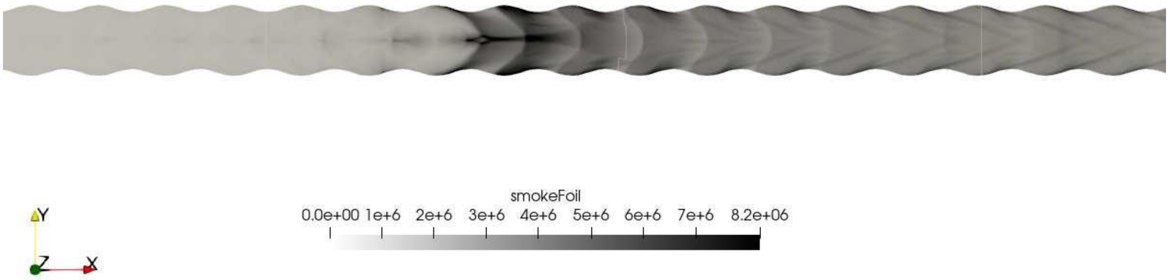

a) $BR = 0.2$

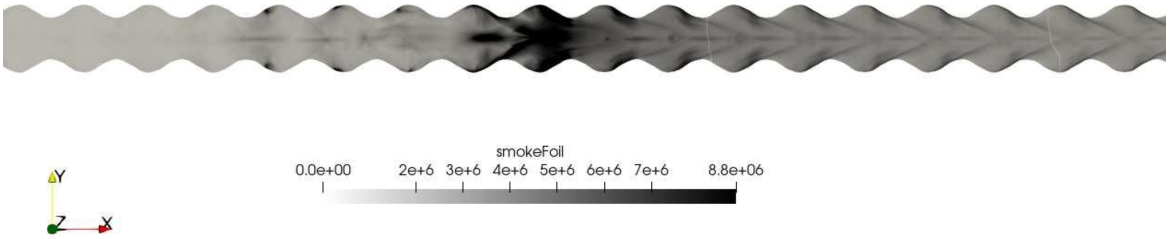

b) $BR = 0.4$

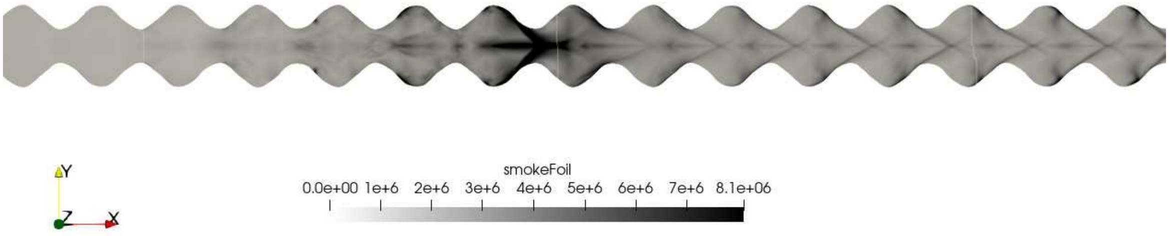

c) $BR = 0.6$

Figure 3.12: Detonation propagation, sootfoils images

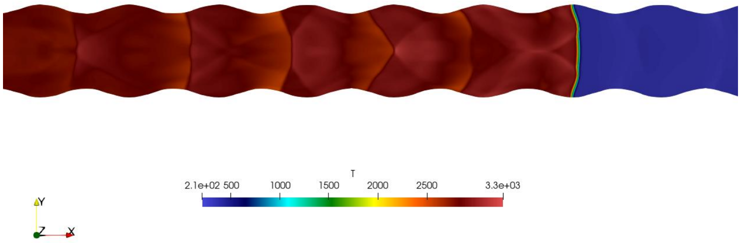

a) $BR = 0.2$

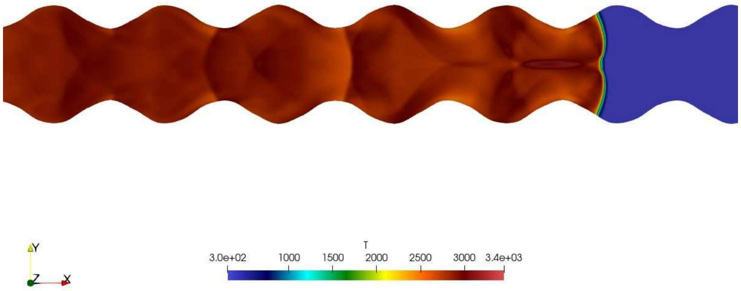

b) $BR = 0.4$

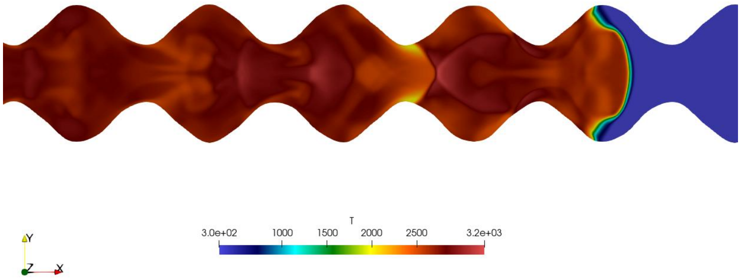

c) $BR = 0.6$

Figure 3.13: Detonation propagation of reaction zone-shock complex

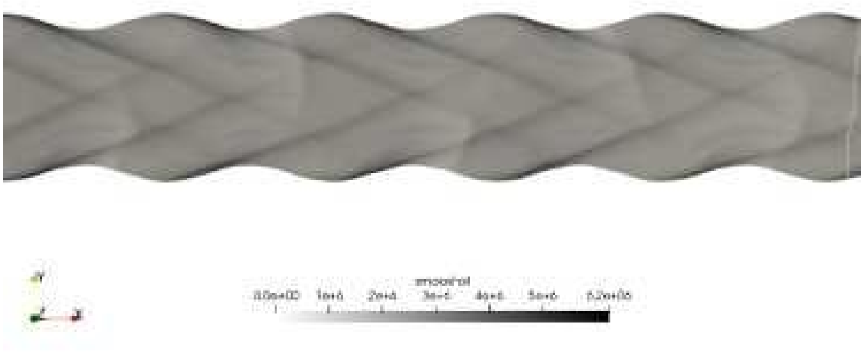

a) $BR = 0.2$

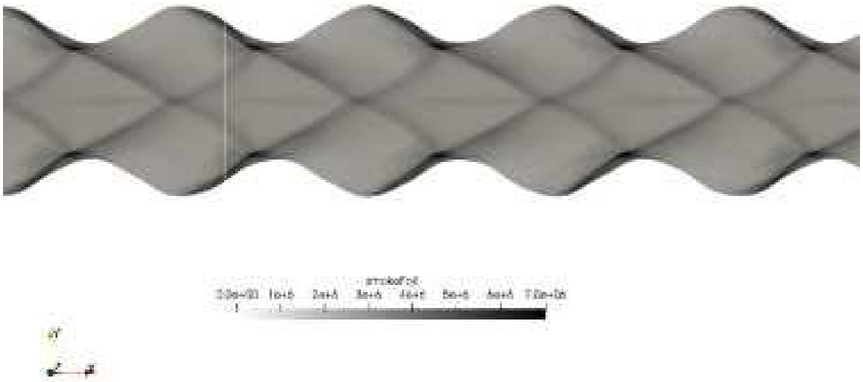

b) $BR = 0.4$

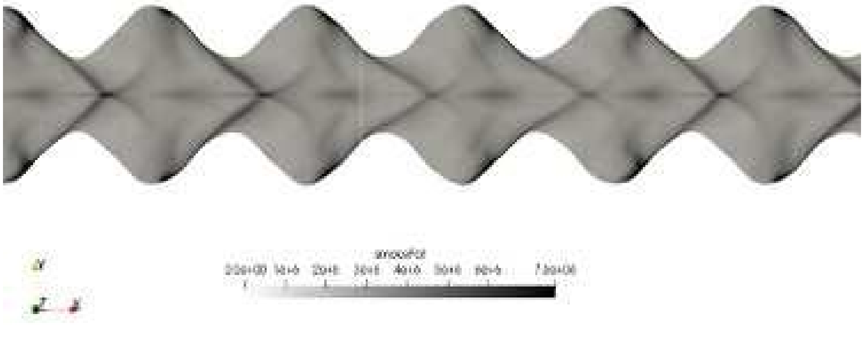

c) $BR = 0.6$

Figure 3.14: Soot foils images of detonation and triple points after DDT

of the detonation wave. The characteristic spatial wavelength λ observed in soot foil patterns is referred as the detonation cell size. Usually measured as the distance between parallel soot traces. This is empirically correlated with other length scales that can also be defined for the transition from deflagration to detonation. Cell sizes are known for a wide range of mixtures and cell sizes and other length scales are strongly correlated with the ideal induction length, L_{ind}, compute using a 1D laminar description of a detonation wave [77]. In our case, the detonation cell, size λ, are 6mm and 7mm for BRs of 0.4 and 0.2. Comparing with the experimentally reported λ for a H2-Air mixture at $p_0 = 100$ kPa and $T_0 = 300$ K from 'Caltech detonation data base', λ=$7-8$mm, our simulations slightly underestimate the value of λ.

3.4 Effects of initial pressure at constants BR

The other case study analyzed, refers to the effects of the change in initial pressure on flame evolution while maintaining a fixed blockage ratio of 0.6. Three values of pressures p_0, are considered, 25, 50 and 100 kPa.

3.4.1 overall dynamics

The evolution distances for comparison were normalized to the distance reached by the first DDT phase (x_{DDT}). In fig. 3.15 and 3.16 is represented $x-t$ diagram and $u-x$ diagram for different initial pressures at the same BR.

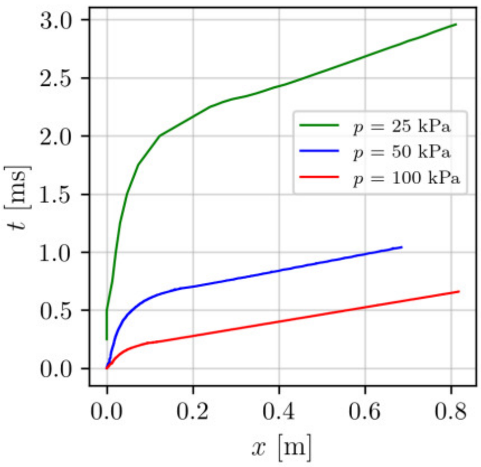

Figure 3.15: $x-t$ diagram at different pressure

In such a way as to compare approximately the same evolutionary state for each difference in pressure. The example in table 3.3 show a distance calculation (x) at 50% of the

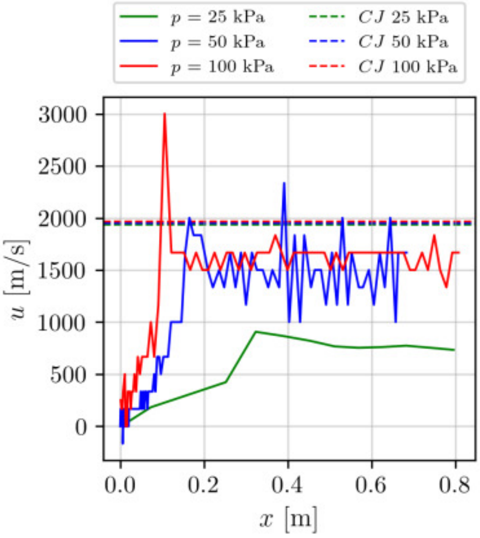

Figure 3.16: $u - x$ diagram at different pressure

p_0 **kPa**	$x_{\mathbf{DDT}}$ (m)	**Evolution** %	$x = x_{\mathbf{DDT}} 0.5$ (m)
25	0.3	50	0.15
50	0.18	50	0.09
100	0.1	50	0.05

Table 3.3: X evolution flame distances at fixed $BR = 0.4$

flame evolution:

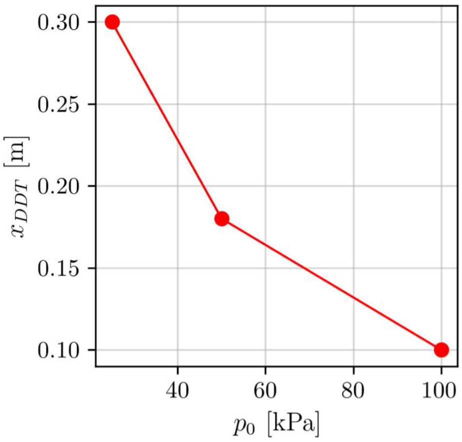

Figure 3.17: x_{DDT} vs. differents p_0

3.4.2 Early/intermediate stages

The initial part of the flame evolution within the channel behaves in the same way as discussed in section 3.3.2 The combustion process begins and drives the flame through the domain, generating pressure waves ahead travelling at the local speed of sound. By decreasing the initial pressure, the flame faces difficulties to reach the same evolutionary state as the initial pressure studied in the previous case of $BR = 0.6$, 100 kPa, for this reason it needs more distance and simulation time to evolve. We can observe a marked increase in pockets of fresh mixture that are not completely burnt as the pressure decreases, allowing a larger flame surface and a higher reaction and induction zone (orange band and green band), fig. 3.18.

3.4.3 Moments prior to DDT

As noted in the case study in section 3.3.3, the moment before a possible detonation is a very delicate condition and set of events, and dependent on several variables. In this particular case, the occurrence of critical conditions that may lead to a detonation also depends on the initial pressure. In fact, taking into consideration an evolutionary state of the flame of 95% with respect to an initial onset of detonation, ($x = 0.95x_{\mathrm{DDT}}$) some considerations can be made in all three cases. As shown in the figure 3.19 below, the topological behavior of the flame is different; at 100 Kpa, the flame begins to take on characteristics close to detonation with the reaction and induction bands being much thinner, and a reduced flame surface. At 50 Kpa the flame surface is larger and has more extensive reaction zone bands, but still approaches near-detonation behavior; Flame-shock interactions are visible and affect the flame shape. For the 25 kPa case, the topology is very different, the flame still has large recirculation zones, and its shape is very different from the other two, the low pressure in this case may have altered the necessary conditions and greatly reduced the flame's ability to accelerate enough to recreate critical conditions for detonation to occur. The fact that the flame is significantly thinner in this case makes it more vulnerable to eddies present in the flow field, and as a result the flame shape changes significantly.

3.4.4 Onset of detonation/detonation propagation

$p_0 = 100$ kPa

As has already been analyzed in section 3.3.4, the case with $BR = 0.6$ and 100 kPa presents a quasi-detonation regime [60]. This regime is characterized by a continuous coupling and decoupling of the reaction zone with the leading shock, as shown in the sequence of pictures, Figs. [20]. Another clear proof of this behavior is represented in the image of the soot foil, fig,[20](c), characterized by a non-distinct definition of the cellular structures left behind by the reaction zone and the shockwave. In fig [20](a) the reaction front advances almost coupled to the leading shock, as soon as the flow enters the diverging section, fig [20](b) the reaction zone-shock complex velocity has a deficit due to heat and energy losses associated with the large area change of $BR = 0.6$, and the front decouples even if only slightly from the leading shock. As the flow passes through the converging section, fig [20] (c) and (d), the front tends to re-couple recovering energy in compression. It has been observed, also in Ciccarelli and Doroofev's review [3], that for larger obstacles the velocity deficit is due to the detonation wave failing and re-initiating as it propagates through the obstructed channel with orifices, a similar outcome to that observe for our wavy channel.

$p_0 = 50$ kPa

By decreasing the initial pressure to 50 kPa, we found a further decrease in reaction zone performance with larger deficits and losses, as we expected. We are always faced with a regime of near detonation with zones of failure and zones of re-initiation that are higher in density and criticality than others, as is shown in the figure of the soot foils, fig. 3.21 at some distance from the first detonation attempt, the cellular structures present a kind of pattern where every two converging/diverging sections the reaction zone-shock complex tries to reach the leading shock ahead, propelled by the explosions of the two shock waves crashing into the centre of the channel section, generating points of high pressure and temperature. Different cellular structures than those observed for 100 kPa case, fig. 3.14(c) soot foils. This trend can also be seen in the sequence of figures, figs. where the evolution of the flame morphology is shown. One can see significantly larger losses and larger distances of the reaction zone-shock complex from the leading shock than in the previous case. In fig. 3.22 (a) one can see a high critical point in the centre of the channel, due to the impact of two or more shock waves, which push the flame only to the centre, generating a central pinnacle, or lead flame tip, as in fig. 3.22 (b), which increases losses. The following figures show how the flame tries to re-couple with the leading shock, until in fig. 3.22 (e), thanks to a more intense explosion in the centre, the reaction zone-shock complex re-couples with the leading shock. This sequence represents the pattern seen in the images of the soot foil, which is constantly repeated until the end of the channel.

$p_0 = 25$ kPa

Continuing to decrease the pressure, we now analyze the last case with a pressure of $p_0 = 25$ kPa. In this particular situation, detonation or quasi-detonation does not occur, but a particular regime called “choked flame” or “choking regime” occurs. A term that is often used to characterize fast flame in ducts with obstacles that travel at a speed just below the isobaric sound speed in the combustion products, as mentioned in the Ciccarelli and Doroofev paper [3], this is also verified by the u-x diagram shown in fig. 3.16. This fast flame regime can be distinguished from quasi-detonation by a relatively low strength lead shock which is not sufficient to cause autoignition of the mixture, where a regular flame is too slow to be responsible for the fast-burning rate required for the propagation at high supersonic speeds. As shown in the sequence of pictures, figs. 3.23, the flame brush surface reaches a maximum of speed at the flame tip and as soon as the combustion products flow velocity reaches the local sound speed, the flow behind the flame tip is choked. Any pressure perturbation generated due to the combustion process cannot reach the flame tip. In fig. 3.23 (a) it is noted that the tip of the flame is far from the leading shock, and how the shock waves that collide crushing in the center of the channel in front of the flame create even more losses and instability, such that the flame will never be able to reach the leading shock ahead. This tendency is also shown in the figure of the soot foils, fig. 3.24 where except for the first attempt at detonation, subsequent attempts fail; No cells are formed as a result.

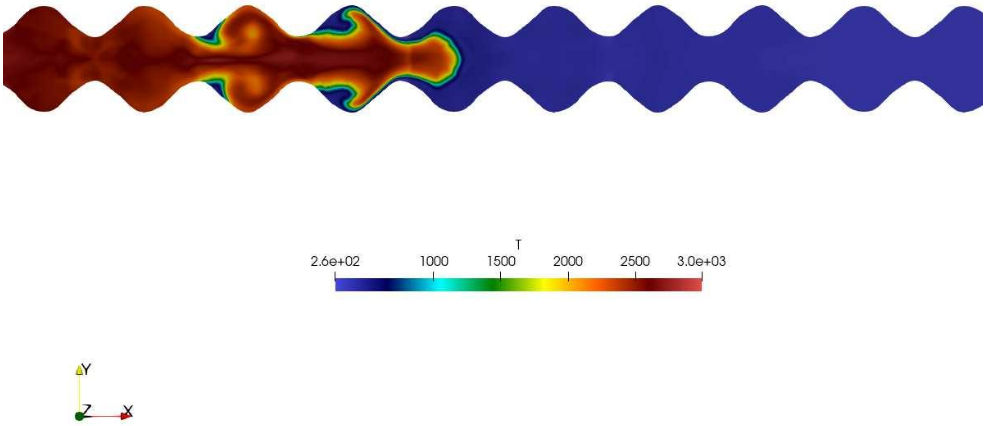

a) 100 kPa

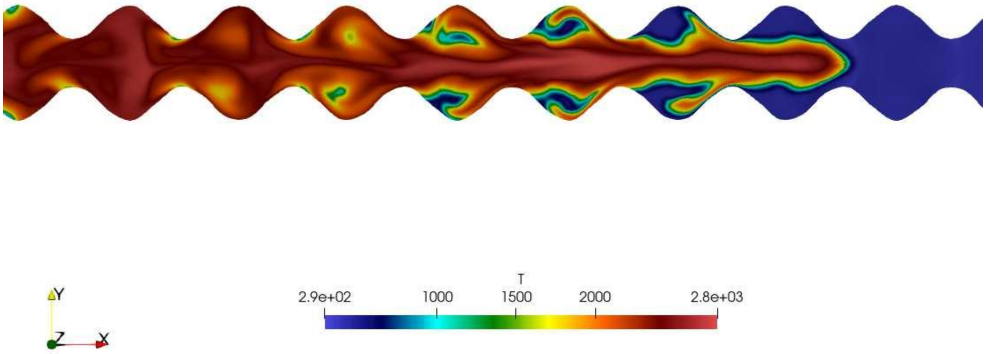

b) 50 kPa

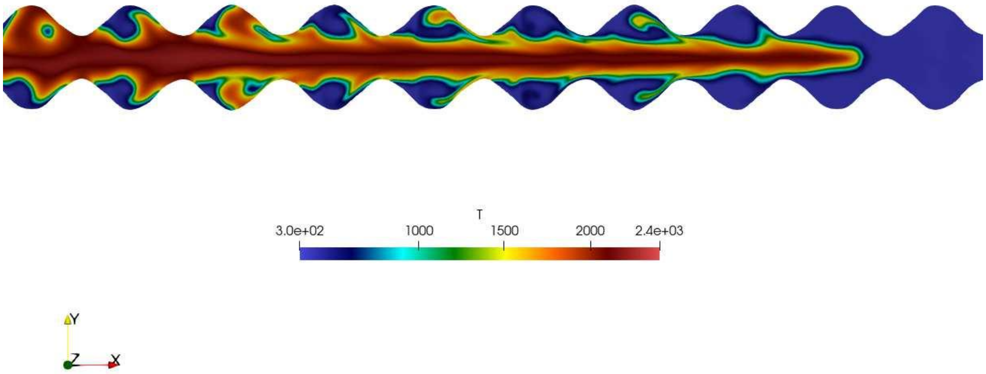

c) 25 kPa

Figure 3.18: 50% evolution of the flame at different pressure at $BR = 0.6$

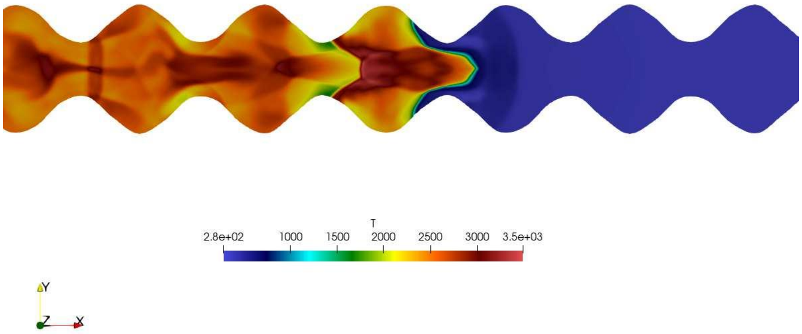

a) 100 kPa

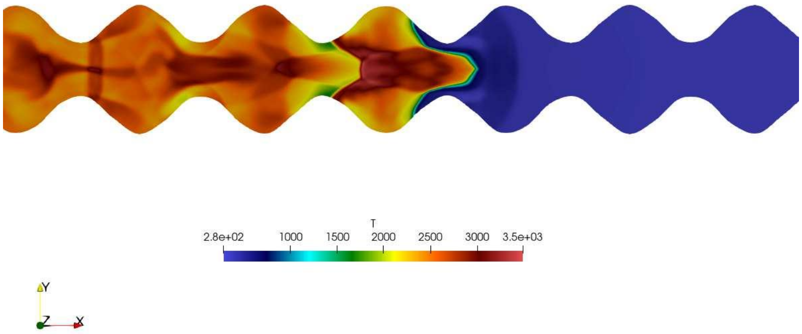

b) 50 kPa

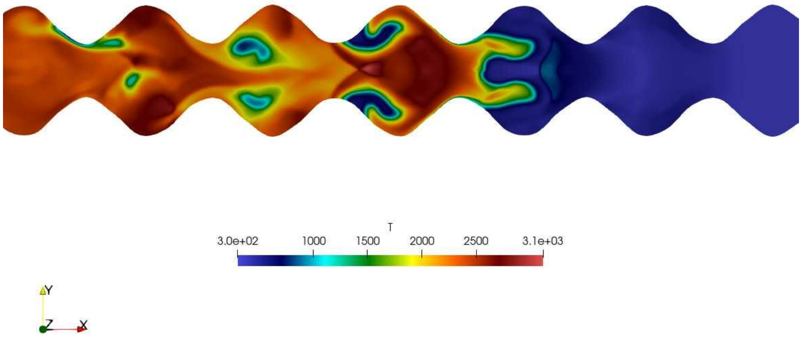

c) 25 kPa

Figure 3.19: 95% evolution of the flame at different pressure

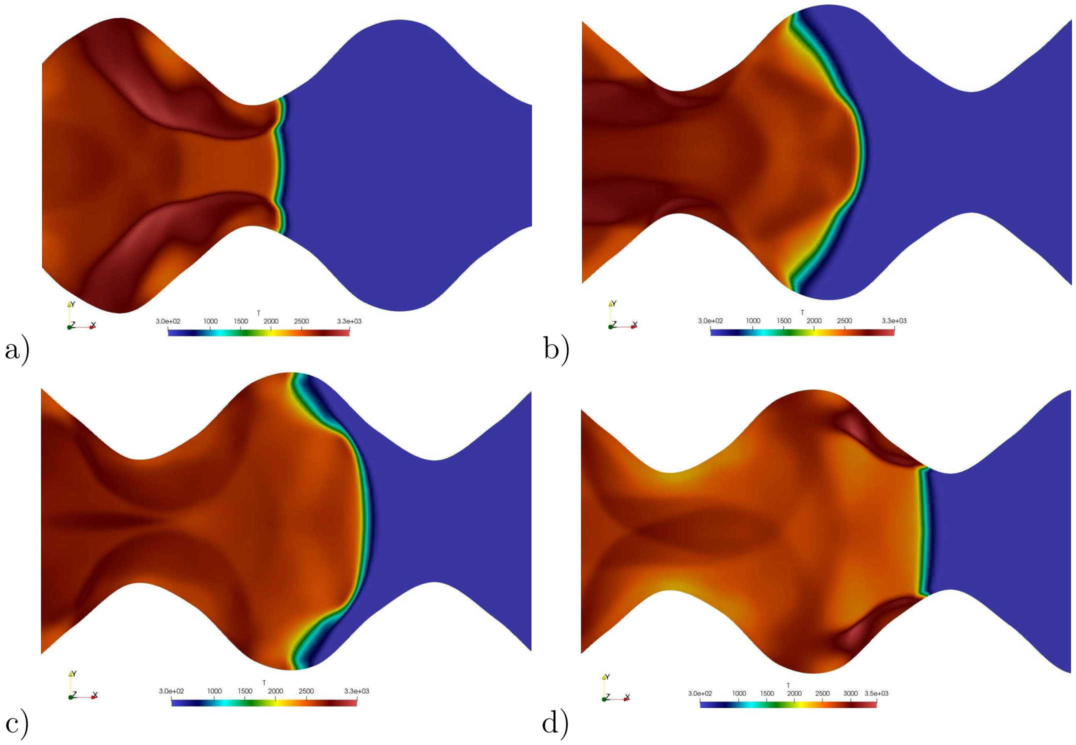

a) b) c) d)

Figure 3.20: Quasi-detonation propagation for $p_0 = 100$ kPa. a) frame at instant $t_{ref} = 6.01 \times 10^{-4}$ s, the Δt between consecutive frames is Δt= 0.2×10^{-5} s. The entire cycle is 6.01×10^{-4} s $<$ t $<$ 6.07×10^{-4} s

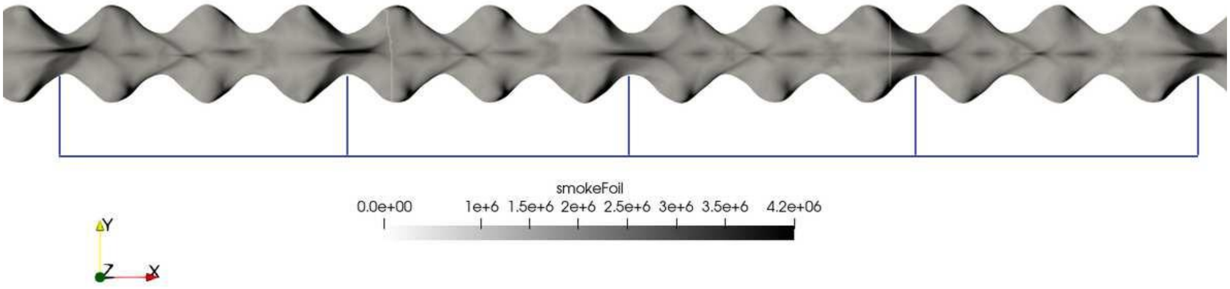

Figure 3.21: Soot foils, Quasi-detonation propagation for $p_0 = 50$ kPa, and pattern of critical points.

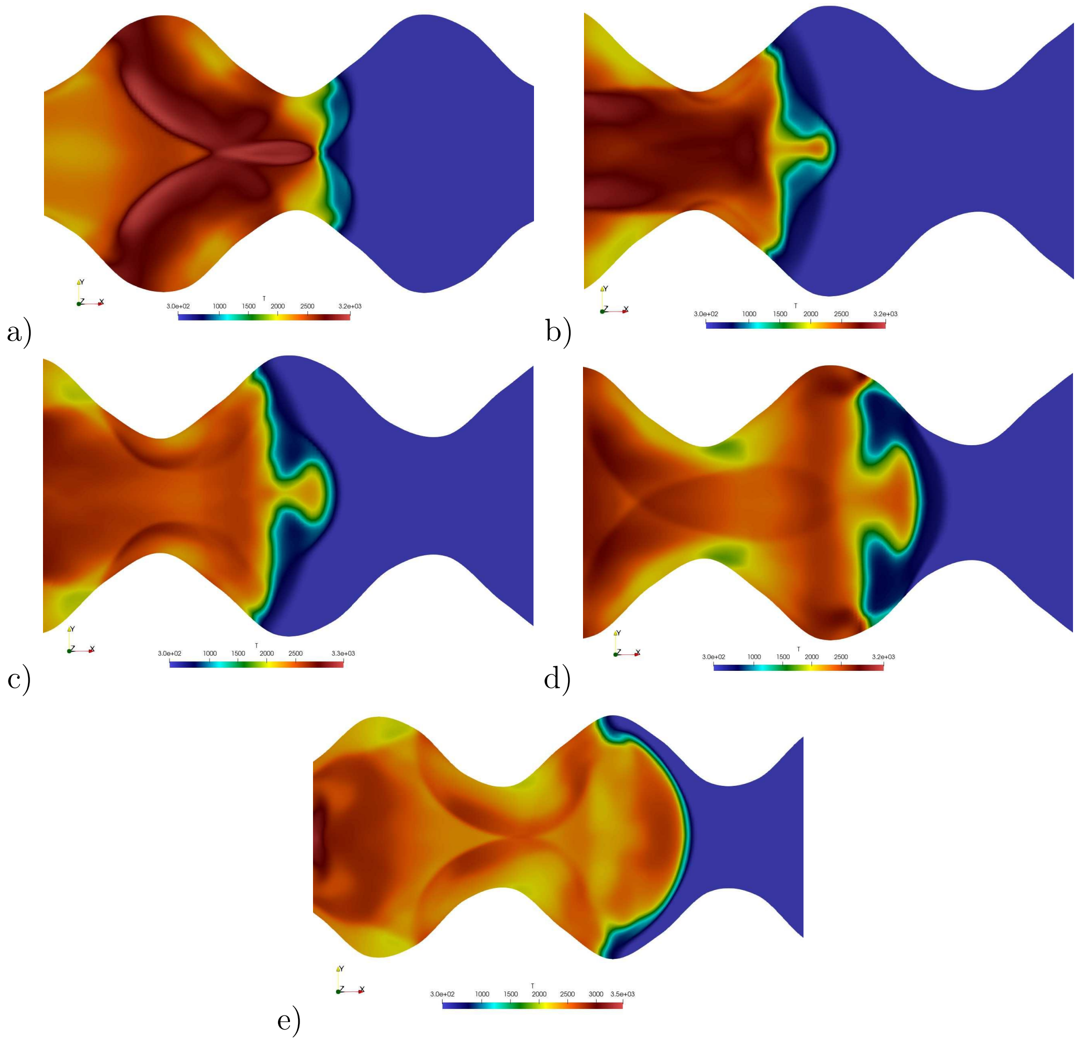

a)

b)

c)

d)

e)

Figure 3.22: Quasi-detonation propagation for $p_0 = 50$ kPa. Δt for each consecutive frames is Δt= 2×10^{-4} s. From picture a) to e) is 7.99×10^{-4} s $<$ t $<$ 8.07×10^{-4} s

a) t=2.71 $\times$ 10^{-3}s

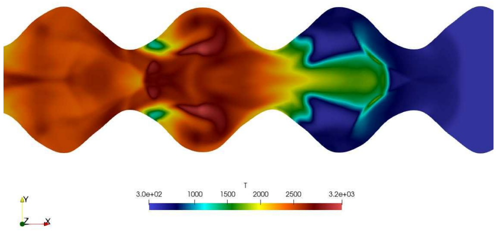

b) t=2.74 $\times$ 10^{-3}s

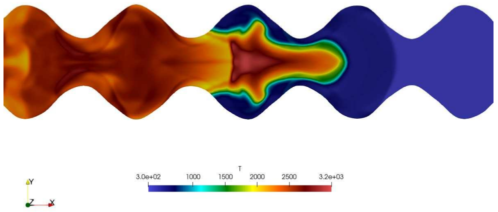

c) t=2.76 $\times$ 10^{-3}s

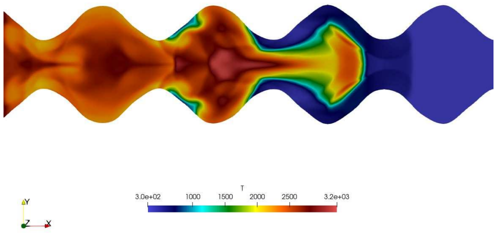

Figure 3.23: “Choking regime” propagation for $p_0 = 25$ kPa

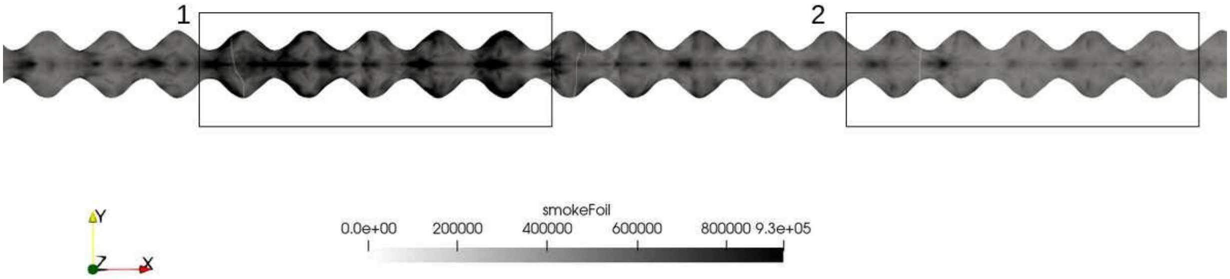

Figure 3.24: Soot foil of “Choking regime” propagation for $p_0 = 25$ kPa

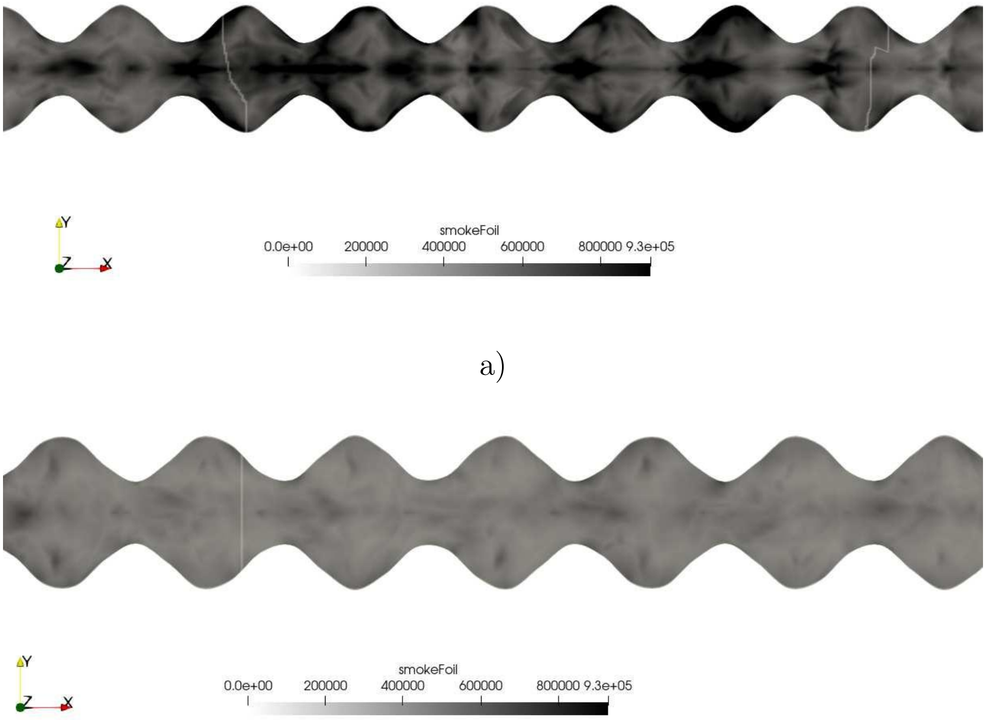

a)

b)

Figure 3.25: Soot foil of “Chocking regime” propagation for $p_0 = 25$ kPa. 1) Zoom part 1, first attempt of detonation; 2) zoom part 2, choking regime propagation

Chapter 4

Unobstructed

4.1 Domain, initial and boundary condition

Once we had tested our solver with the "obstructed" wavy channel. We decided to analyze the case of an unobstructed straight channel, studying the evolution of the flame, and testing the effects of viscous heating. In order to enhance the effects of the boundary layer, we reduced the size of the channel, to a height of 1 mm, maintaining the total length of 1 m and leaving the initial ignition conditions unchanged, and a pressure p = 100 kPa and temperature T = 300 K. In this case the flame was ignited by imposing only one hemi-spherical region of radius $r = 0.00025$ m, as shown in fig. 4.1.

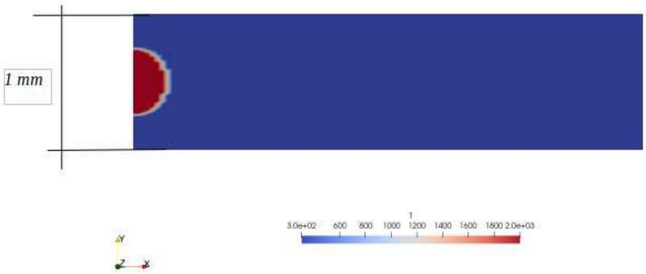

Figure 4.1: Domain, initial and boundary condition with $L_x = 27778$ (resolution along x direction)

L_x	$x_{\mathbf{DDT}}$ (m)	**Evolution** %	$x = x_{\mathbf{DDT}}0.5$ (m)
7895	0.27	50	0.14
15790	0.45	50	0.23
27778	0.62	50	0.31

Table 4.1: X evolution flame distances at fixed $BR = 0.4$

4.2 Effect of resolution on run-up distance

4.2.1 Overall dynamics

As the mesh resolution was rather coarse at this size, we considered and analyzed 3 different cases according to the type of qualitative mesh resolution, increasing the number of cells along the x-direction (L_x) by a factor of two for each case. By normalizing, as in the previously studied cases, the distance reached along the channel, of the onset of detonation, one can compare the various cases to the same dynamic evolution of the process, as represented in the example n. 2 and table 4.1, fig. 4.3, and then computing $x - t$ diagram for each case, fig. [28].

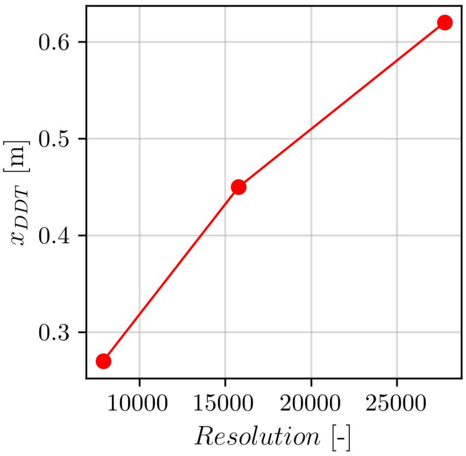

Figure 4.2: x_{DDT} vs. different resolution

4.2.2 $L_x = 15790$; Early/intermediate and moment prior to DDT

The comparisons between the various cases are not of much interest as the topology of the flame remains the same only seen at a different resolution. However, by increasing the resolution along the x-direction, and thus increasing the computational cost of the simulation, we obtained different x_{DDT} distances specifically, x_{DDT} occur further in the

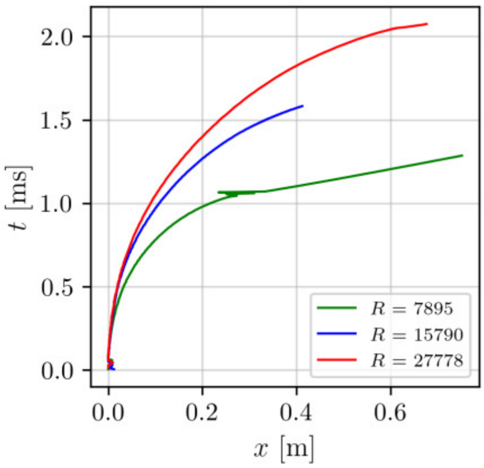

Figure 4.3: $x - t$ diagram for different resolution

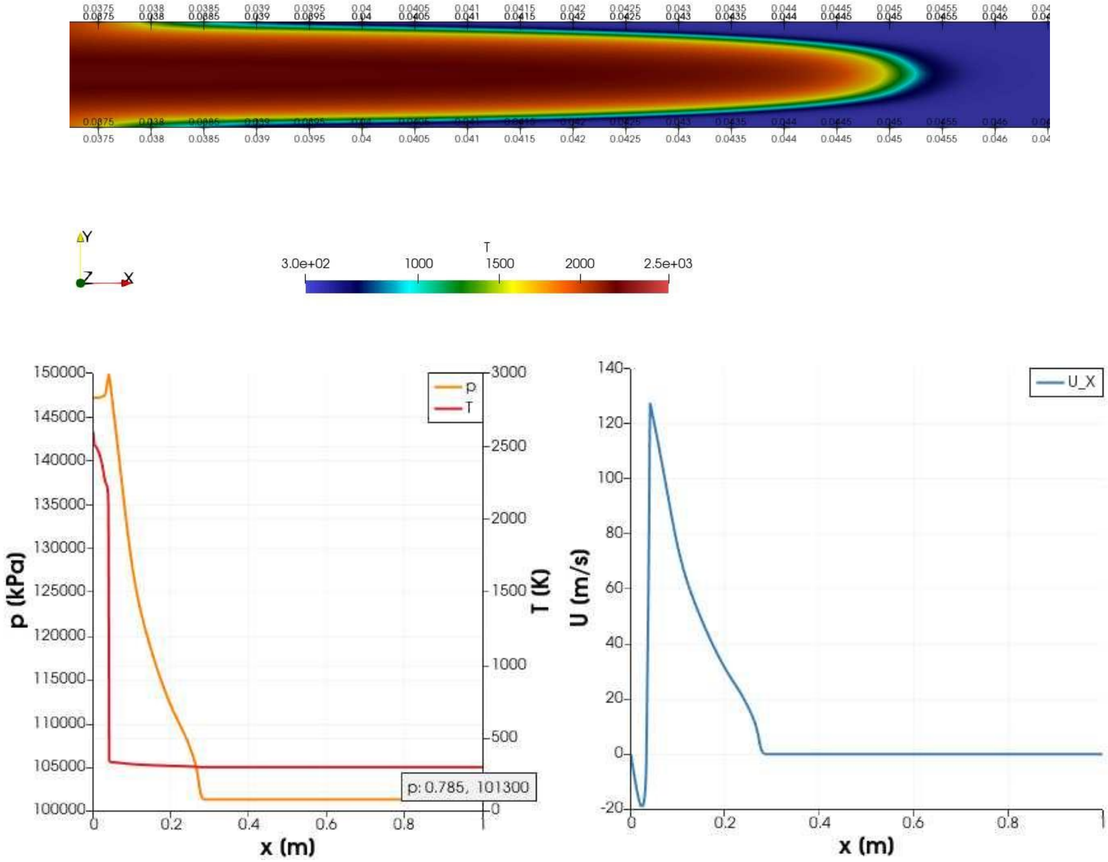

Figure 4.4: $L_x = 15790$ a) Early stage of flame, 10% of evolution,($p - T$ diagram, flow field at showing frame and $Ux - x$ diagram, flow field at showing frame)

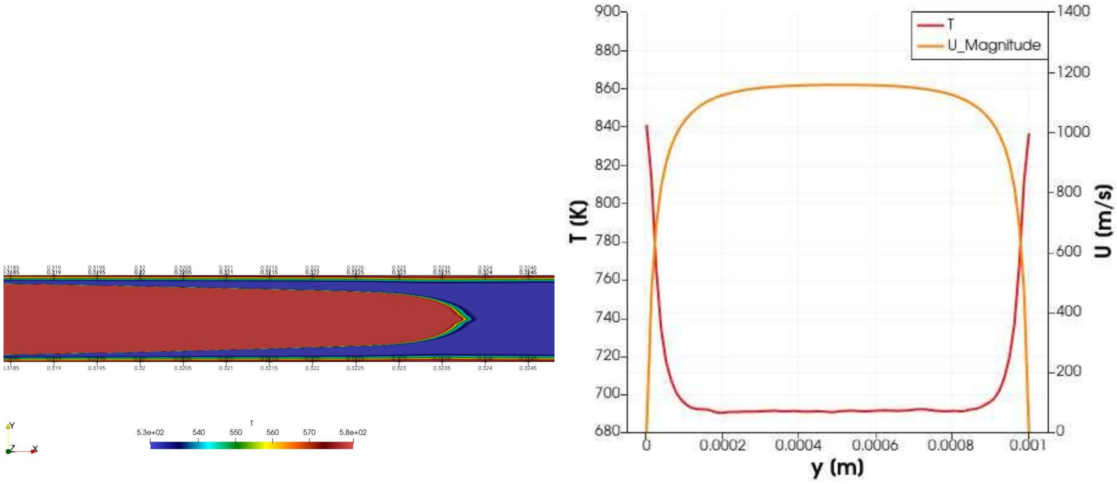

Figure 4.5: $L_x = 15790$ b) Intermediate stage of flame, 70%,($T-U$ diagram, effect of walls heating along height of the channel at showing frame)

channel as the resolution increased, as shown also in the $x-t$ diagram figs. [28]. We therefore decided to focus on only one of the cases, in order to study the effects of the boundary layer and the evolution of the flame and how transition to the detonation takes places. We considered the case of $L_x = 15790$ because it is the case for which we recorded the most time steps in the simulation.

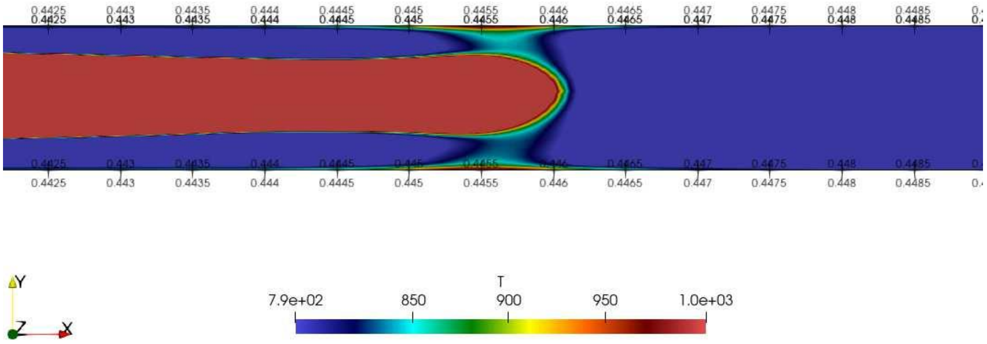

Figure 4.6: $L_x = 15790$ c) Moments prior DDT, 99%

Taking this case into consideration, the evolutionary analysis of the process will also be identical for the other two cases. In the early stages of the flame (between 10-50% of the evolution). The behavior is different as that observed in the wavy channel in section 3.3.2, since no shock wave interaction occur. We are in the deflagration regime, the flame is accelerating, and the induction and reaction zones are clearly visible, as in fig. 4.4. In the intermediate evolutionary state, we can observe a slight effect of the boundary layer slowly beginning to increase its temperature and its thickness, creating a kind of convergence condition that drives the flame ahead, as in fig.4.5. Very close to detonation (moment prior DDT) the necessary conditions for the transition are established, the boundary layer plays a fundamental role, generating a critical point by reflecting the shock waves formed downstream of the flow, the flow is as if sucked in and then shot forward, in what will become a stationary detonation regime, fig. 4.6.

4.2.3 Onset of detonation

We have acquired detailed images of how the detonation occurs for this case. The sequence of images, figs. 4.7, shows a very short simulation range involving a small portion of the channel length ranging from $0.4476 < x < 0.450$ mm, in this minimal distance the detonation takes place. Following the sequence of the images: In fig. 4.7(a) it can be seen that the shape of the flame changes considerably, swelling towards the edges, in fig. 4.7(b) one of the critical points on the upper edge of the channel was probably subjected to an explosion with boundary layer. These detonation points are characterized by temperatures and pressures, as in fig. 4.8, which releases a strong shock wave, this represents detonation onset for this case. Fig. 4.7(c), shows that the lower edge also begins to present a critical point that seems to explode, after which the two shock waves generated by the hot spots, starting from the edges, expand, pushing the flame front, until they impact roughly in the center of the channel, creating an extremely intense zone which initiates the detonation propagation regime, fig. 4.7(e).

4.2.4 Detonation propagation

The detonation propagation regime remains the same as in the case of the corrugated channel in Section 3.3.5. The figures below, fig. 4.9, show the morphology of the reaction front, where we can see that the reaction and induction zones are very thin. The diagrams show the flow field trends of temperature pressure and velocity fig. 4.9(a). The soot foils fails does not show the cellular structure of the detonation because the height of the channel is small compare to the cell size of the mixture.

4.3 Adaptive mesh refinement -3D channel

Once we experienced the unobstructed channel, preliminary tests for a 3-D channel (5 mm × 5 mm cross section; 1 m in length) using Adaptive Mesh Refinement (AMR) are being carried out. Initially, a general overview will be given on AMR in the subsection 4.3.1.After

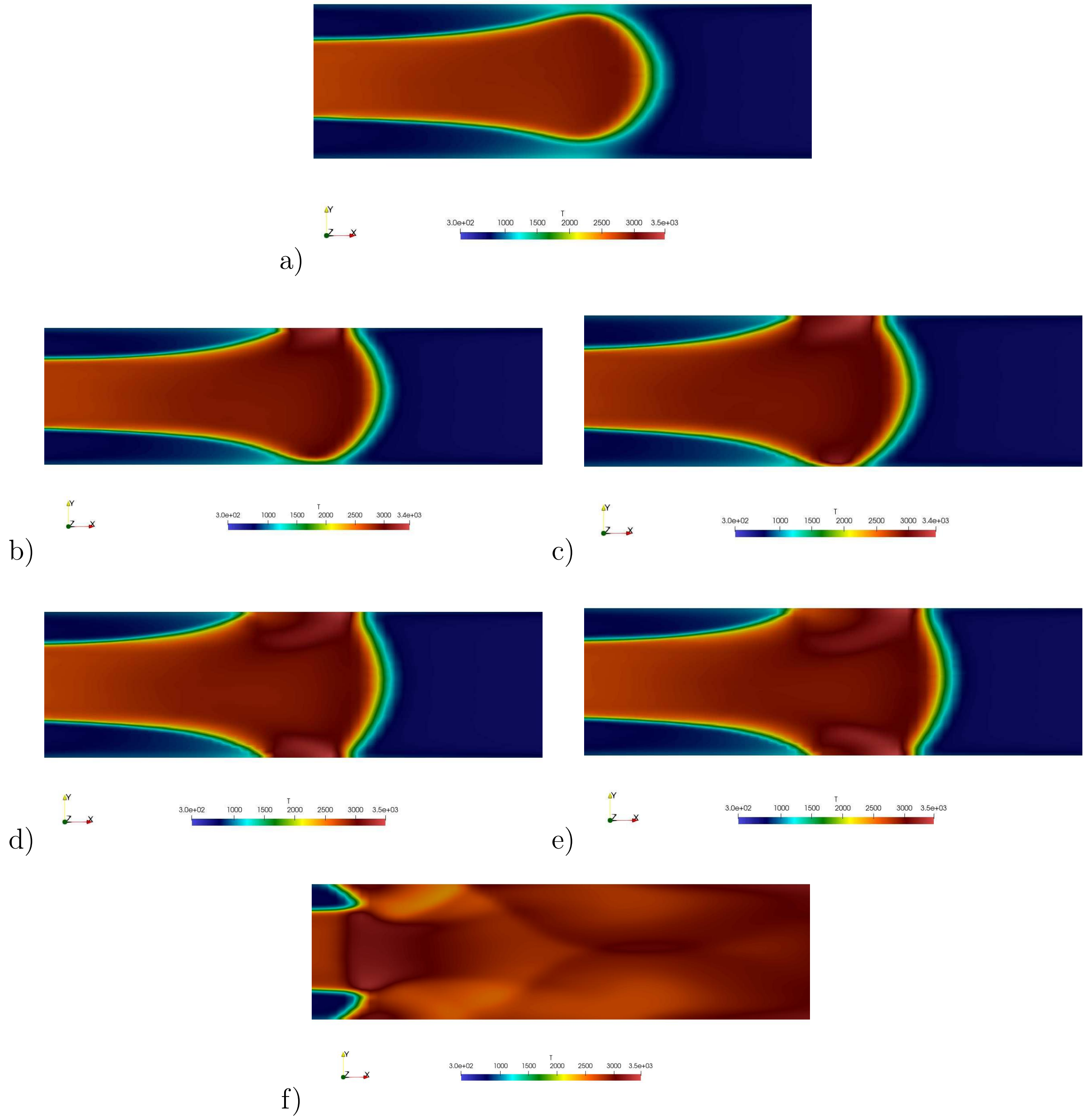

Figure 4.7: Sequence of critical explosion points turned in DDT, 0.4476 m $<$ x $<$ 0.450 m

that, an explanation of the implementation of AMR in OpenFOAM at the code level within our executable will be given in the subsections 4.3.2, 4.3.2, 4.3.3, 4.3.4. How the libraries and functions are called up, how the dynamic mesh is constructed, and how the mesh is refined by creating and updating cells. In the subsection 4.3.5, we give an explanation of how the dynamic mesh dictionary is used to control AMR within our case stud. Finally, in the section 4.4 and subsections **??** **??**, we will discuss how the solver acts on the mesh

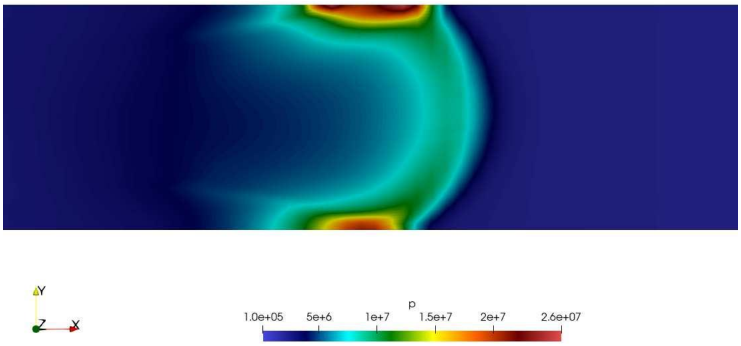

Figure 4.8: Critical pressure detonated points, 0.4476 m < x < 0.450 m

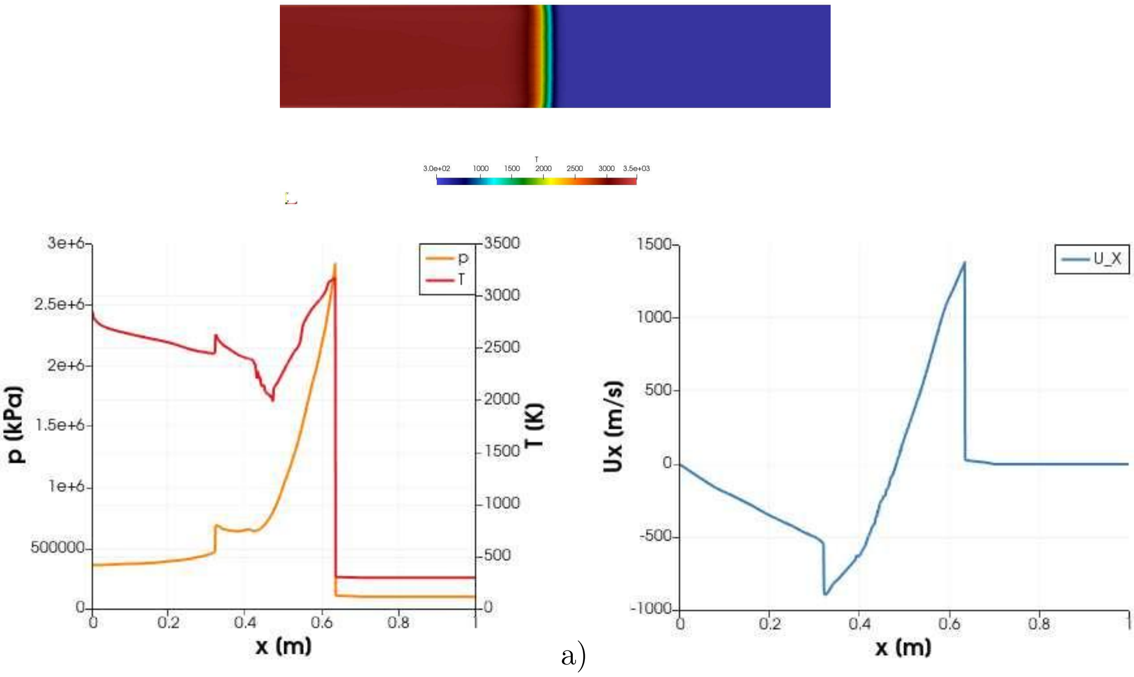

a) a)

Figure 4.9: Detonation propagation regime a) p−t and Ux diagram at Detonation propagation regime

refinement in our case of interest, and the first results obtained will be shown visually.

4.3.1 Adaptive mesh overview

One of the key aspects of numerical simulations is the meshing. Meshing refers to discretization of the domain over which simulation occurs. Every, discrete numerical scheme is limited greatly by the constraints on the mesh. The size, shape and orientation of mesh elements, play a major role in the stability and accuracy of the numerical scheme. They also directly influence the computational cost, as more elements lead to direct increase in number of computations.

The partial differential equations that govern fluid flow and heat transfer are not usually amenable to analytical solutions, except for very simple cases. Therefore, in order to analyze fluid flows, flow domains are split into smaller subdomains (made up of geometric primitives like hexahedra and tetrahedra in 3D and quadrilaterals and triangles in 2D). The governing equations are then discretized and solved inside each of these subdomains. Typically, one of three methods is used to solve the approximate version of the system of equations: finite volumes, finite elements, or finite differences. Care must be taken to ensure proper continuity of solution across the common interfaces between two subdomains, so that the approximate solutions inside various portions can be put together to give a complete picture of fluid flow in the entire domain. The subdomains are often called elements or cells, and the collection of all elements or cells is called a mesh or grid. The origin of the term mesh (or grid) goes back to early days of CFD when most analyses were 2D in nature. For 2D analyses, a domain split into elements resembles a wire mesh, hence the name.

The most basic form of mesh classification is based upon the connectivity of the mesh: structured or unstructured.

- **Structured** A structured mesh is characterized by regular connectivity that can be expressed as a two or three dimensional array. This restricts the element choices to quadrilaterals in 2D or hexahedra in 3D. The regularity of the connectivity allows us to conserve space since neighborhood relationships are defined by the storage arrangement. Additional classification can be made upon whether the mesh is conformal or not.

- **Unstructured Meshes** An unstructured mesh is characterized by irregular connectivity is not readily expressed as a two or three dimensional array in computer memory. This allows for any possible element that a solver might be able to use. Compared to structured meshes, the storage requirements for an unstructured mesh can be substantially larger since the neighborhood connectivity must be explicitly stored.

The number of elements in mesh, or rather the size of the mesh is decided by the length scales of the process being simulated. Length scales are a good measure of a lower limit on the resolution(points per unit length). Thus, a major problem arises when the size of the computational domain is orders of magnitude larger than the length scales. Meshing the whole domain based on desired length scale resolution would lead to computationally complex or even unfeasible meshes. Most of these, cases have a relatively small zone of interest, where the gradients are steep while most of the domain, is slow varying. Thus, one can get away with, a proper resolution in the zone(s) of interest while keeping rest of the domain relatively coarse. Since, the zone(s) of interest usually evolve with time, through the simulation, the mesh has to change accordingly.

This, is precisely the concept of adaptive mesh, or more generally dynamic mesh. the difference between a dynamic and adaptive mesh is matter of motion. Usually dynamic mesh, deal with a moving zone of interest, where the motion can be calculated, without any addition computational complexity. Adaptive meshes on the other hand, fit only according to the zone of interest. So, some computational maybe be saved by using moving meshes in cases of simple motion, but Adaptive meshes tend to be more general.

There has been a great deal of recent interest in local mesh refinement procedures for solving steady and time-dependent partial differential equations. Such techniques are being used to calculate solutions having prescribed levels of accuracy. In order to avoid unnecessary computation and to achieve the required accuracy in an optimal, or at least an efficient, manner, it is desirable to have a finer mesh in regions where the solution is varying rapidly and a coarser one in regions where it is varying slowly. [78]

Adaptive mesh implementation follow the following algorithm.

1. Identify zone of interest
2. Identify cells, that can undergo splitting(refinement)
3. Refine the cells, and map the fluxes

A similar loop is employed to simultaneously combine(unrefinement) in places that are no longer of interest.The unrefinement is necessary, and better kept separate from the refinement process to have more control on the mesh adaption and avoid interference in mesh altering operations. The zone of interest is usually described by a by user prescribed field, which much like a distribution function peaks in and around the zone of interest. In the identification step, the parts of mesh with higher field value are marked for spliting. The processes of AMR will be explored in the coming sections with a focus on OpenFOAM implementation and its application in the solver developed.

4.3.2 Implementation of AMR in OpenFOAM

OpenFOAM provides adaptive mesh support with the help of *dynamicFvMesh* library. This library, allows for both mesh motion and adaptive meshes. The *dynamicFvMeshRefine* is inherited class which manipulates the *dynamicFvMesh* object(mesh), based on parameters defined by user. *dynamicFvMeshRefine* reads the *dynamicMeshDict* present in the *case/constant* to read the parameters required. The *dynamicFvMeshRefine* has member function which use *hexRef8* class to refine and unrefine the cells. To understand the exact working, first the parts of the mesh and the way they are processed in OpenFOAM, need to analyzed. Then the libraries and function calls for AMR, are merely a code construct.

Mesh elements

A mesh, consists of points, cells faces and edges(4.10). Each of them are stored as separate list with relational tables mapping for each cell, points, edges and faces. This allows hierarchical operation on the cell. So every time refinement occurs, the operations end involves simply a insert in cell list and update of cell neighbours. This separates cell level operations from mesh level operations, making the implementation more modular. The benefit of such modularity will become apparent with cell spliting in 4.3.4.

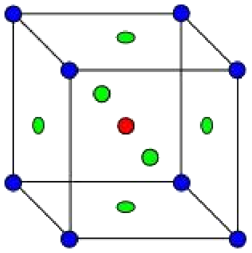

Figure 4.10: The mesh elements, the Cell with Red:Cell centre, Green:Faces, Blue:Corners, Black:Edges

In terms of code implementation. The elements are defined as:

- Points: represented by object *point* is basically a *std::vector*
- Edge: represented defined as a pair of two points.(label pair in the mesh pointField)
- Face: represented as list of Mesh vertices; A containers of edges and points
- Cell: A cell is defined as a list of faces with extra functionality.

Note: that only hexahedral cells are supported for AMR, although OpenFOAM has the ability to process other kind of cells as static meshes.

4.3.3 Libraries and Function calls

The implementation of AMR algorithm happens with the help of the library files mentioned at the beginnings of 4.3.2. The inclusion of header *dynamicFvMesh.H* ensures the mesh is dynamic and can be changed during runtime. The mesh is created by the *createDynamicFvMesh.H* header.

1. The solver only needs to execute ***mesh.update()***, which is part of the *dynamicFvMesh* library. The *dynamicFvMeshRefine* reads the *dynamicMeshDict* in *constant* directory. The *dynamicMeshDict* contains the parameters on which refinement and unrefinement takes place (Code 1). The effects of these parameters on the mesh refinement are discussed in the 4.3.5.
2. The solver determines the cells that need to be refined by the *selectRefineCandidates()* in *dynamicFvMeshRefine*. The cells are selected based on the field and maximum number of cells specified in the *dynamicMeshDict*. One additional constraint on the refinement is *nAnchorPoints* must have a value of 8, which is determined based on cellLevel and pointLevel of the cell. These are parameters of Cell and changes based how many time the cell has undergone spliting. To find the value of nAnchors for a given cell, a loop is taken over all the points of the cell and if the pointLevel is less than or equal to cellLevel for a point, then this point is added to the nAnchors. In the dynamicRefineFvMesh file, the cellLevel and pointLevel are defined such that each cell has a cellLevel starting with 0 for the original cell and if the cell is refined once then this number becomes 1 for each new cell and so on. The value of pointLevel is similarly defined.[79]
3. Once the the cells are marked to split, the *refine()* function is called, which inturn calls *setRefinement()* in *hexRef8.H*. This proceeds to split the cells as described in the next section.
4. *selectUnrefinement()* is called which based on the *pointLevel*, *nBufferLayers* and *unRefineValue* in the *dynamicMeshDict* marks points that can be deleted.
5. Unrefinement occurs by calling the *unrefine()* function, which calls the *setUnrefinePoints()*. This function removes the points selected by the function *selectUnrefinePoints()* and their connected faces and points.
6. Finally, the fields are mapped from the old to the new mesh. The values at the centroid are mapped by taking the average for the small cells.[79]

4.3.4 Cell Splitting

The refinement step is cell operation and occurs after the cells which need to be split are marked as explained in Section 4.3.1. The refinement occurs as follows:

1. For each marked cell add a cell midpoint

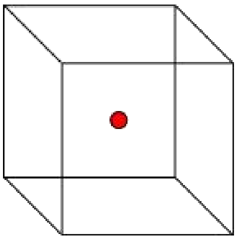

Figure 4.11: The Cell centre marked to add point

2. Identify Faces and Add points in Face Centres. The faces of the cell are obtained from the relational table, and the face centres are in marked to inserted.

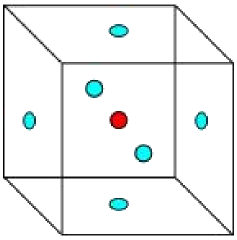

Figure 4.12: The Face centres marked to add points

3. Add Edge midpoints, to each edge

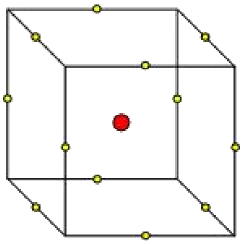

Figure 4.13: The Edge centres marked to add points

4. Split the face in 4 new faces, each face is assigned a neighbour and owner cell.

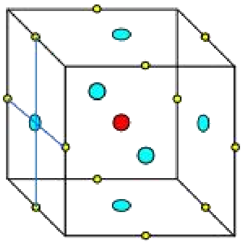

Figure 4.14: The Face split.

5. Internal faces are added to the cell by connecting the points in the center of two neighboring faces, the point in the center of the edge that connects the faces,and the point in the center of the cell, Therefore, a neighbor and an owner cell are assigned to each face.

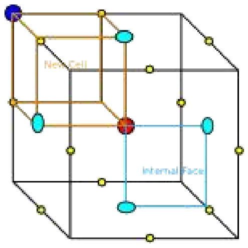

Figure 4.15: The creation of internal face and new cells.

6. Now,the various field can be mapped onto the new cells. The fields are mapped from the old mesh to the new mesh as an initial condition to speed up the computational process. The field value at the centre of a cell in the original mesh is transferred to the new cells by assigning them the same values.

4.3.5 Dynamic Mesh Dictionary

As discussed in the 4.3.3, the mesh manipulation is controlled through the dictionary file *dynamicMeshDict*. The *dynamicRefineFvMeshCoeff* are used to control the AMR as follows.(Code 1)

- **refineInterval** is used to control the frequency of refinement. In cases, where the temporal variation is slow, the interval (in time steps) may be changed to higher values.

- **field** is a scalarField which is part of the solver and represent the zone of interest. The **upperRefineLevel** and **lowerRefineLevel** are the limits in which to refine. Any field values below the lowerRefineLevel will trigger mesh refinement. Any field values above the upperRefineLevel will trigger mesh coarsening.

- **unrefineLevel** This specifies the max number of times the cells can be coarsened. The level you specify is really a power of 2. So in this case, the unrefineLevel states that cells can increase by a maximum factor of $2^{10} = 1024$ times their original size. This gets to specify a maximum coarsening limit. You typically want this to be a large number of levels.

- **nBufferLayers** is the number of buffer layers between levels around a refined cell. This specifies how many layers the mesh must hold a cell size before proceeding to the next level of refinement (or coarsening). Typical ranges are between 1 - 4. A good starting value is 1.0. This is used to control the transitions between cell sizes and to eliminate any artificial pressure waves due to drastic changes in cell size.

- **maxRefinementLevel** is the maximum number of layers of refinement that a cell can experience. This is similar to the unrefineLevel, only now we are considering refinement, not coarsening. Again, the refinement level specifies a power of 2. So a max refinement of 3 is $2^{-3} = 0.125$ times the original cell size.

- **maxCells** is the max number of cells allowed in the mesh. The dynamic refinement will not exceed this maximum number of cells in your domain.

- **correctFluxes** is a list of fields that require flux correction, with matched velocity field. As refinement splits cells that already have field definitions within them, correctFluxes list specifies which fields need fluxes correct for the new cell faces.Fluxes changed on faces get recalculated by interpolating the velocity. Using 'none' on surfaceScalarFields prevents reinterpolation.

- **dumpLevel** is switch to outuput the cell Level as cell array. Can be used to debug the and visualize the distribution of of refined cells in the doamin.

```
dynamicFvMesh   dynamicRefineFvMesh;//staticFvMesh is used for static mesh

dynamicRefineFvMeshCoeffs
{
    // How often to refine
    refineInterval  1;
    // Field to be refinement on
    field           normalisedGradT;
    // Refine field inbetween lower..upper
    lowerRefineLevel 0.1;
    upperRefineLevel 1.0;
    // If value < unrefineLevel unrefine.
    unrefineLevel   0.05;
    // Have slower than 2:1 refinement
    nBufferLayers   1;
    // Refine cells only up to maxRefinement levels
    maxRefinement   3;
    // Stop refinement if maxCells reached
    maxCells        2000000;
    // Flux field and corresponding velocity field. Fluxes on changed
    // faces get recalculated by interpolating the velocity. Use 'none'
    // on surfaceScalarFields that do not need to be reinterpolated.
    correctFluxes
    (
        (phi_0 none)
        (phi none)
    );
    // Write the refinement level as a volScalarField
    dumpLevel       true;

}
```

Listing 1: Dynamic Mesh Dictionary

4.4 Implementation in solver

In the solver developed can be used directly with minor changes to libraries (Code 2). The dynamic mesh header files and respective library binary code must be made available during the build process for the new solver to work. To include the headers and link the libraries, the MAKE/OPTIONS file needs to be modified by adding the following ”include” lines:

/dynamicMesh/lnInclude and */dynamicFvMesh/lnInclude*, then the application is linked with dynamic mesh libraries by adding the following "linking" lines to MAKE/OPTIONS: *-ldynamicMesh* and *-ldynamicFvMesh*. After these changes, we begin by including the *dynamicFvMesh.H* which and create a dynamic mesh with *createDynamicFvMesh.H*. In case of this solver we chose to use the normalized gradient of temperature as it captures the flame rather accurately. The limits of $[0.1, 1]$ is chosen, based on (Figure 4.17). This interval of normalized gradient best captures the temperature gradient hence the flame. The implementation now reduces to ***mesh.update()***. The solver, before each time step undergoes AMR (due to $refineInterval = 1$), since the zone of interest is moving and the temporal changes have significant effect in case of reacting flows. The general rule of thumb, in the study of laminar flames is to ensure, 15 to 20 points per flame thickness, for proper resolution of the problem. This conditioned is well satisfied as seen in Figure

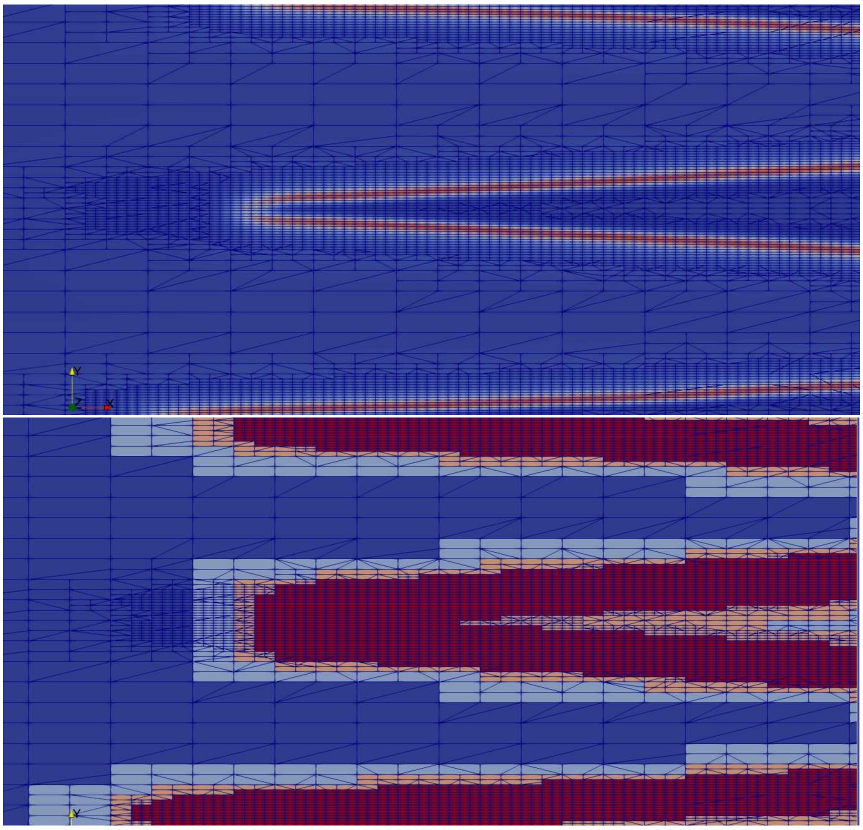

Figure 4.16: The cell levels and mesh size across the normalisedGradT

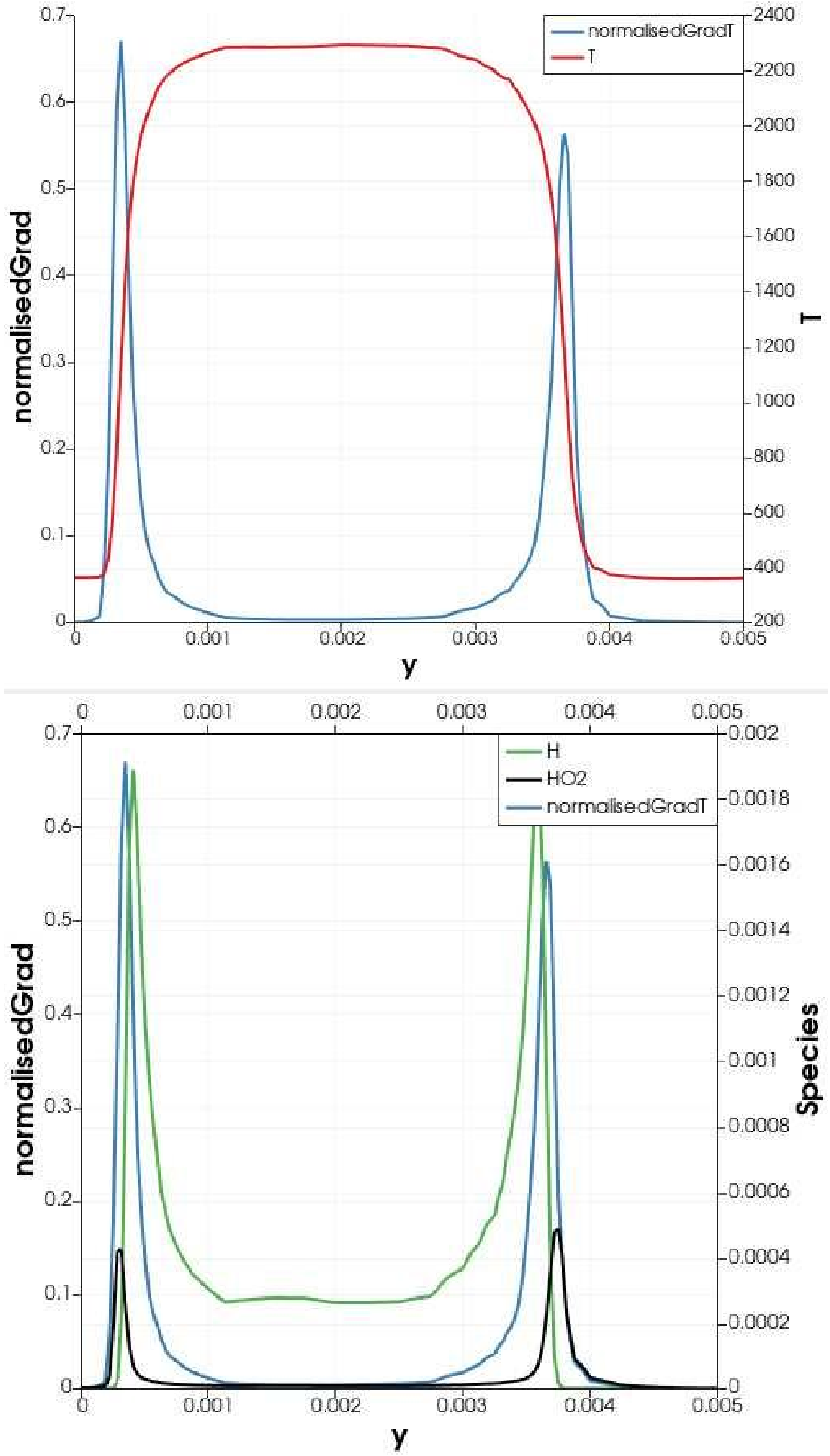

Figure 4.17: Normalised Gradient vs. Temperature and species along y direction; (height of the channel)

```
...
#include "DynamicFvMesh.H" //included  for dynamic Mesh class.
...
    int main(int argc, char *argv[])
    {
    ...
    //#include "createMesh.H" - for a Static Mesh
    #include "createDynamicFvMesh.H" // Creating the dynamic  mesh
    ...
    while (runTime.run())
    {
        ...
        tmp<volScalarField> tmagGradT = mag(fvc::grad(T)); /* store temporarily the
        magnitude of the gradient of temperature*/
        volScalarField normalisedGradT(
            IOobject
                (
                ...
                ),
            tmagGradT()/max(tmagGradT())
           );// create a new normalized gradient of Temperature
        tmagGradT.clear(); // destroy the temporary field
        ...
        //AMR

        scalar timeBeforeMeshUpdate = runTime.elapsedCpuTime();

        mesh.update(); //This the main call for AMR
        //To display the time elapsed in changing the mesh
        if (mesh.changing())
        {
        Info<< "Execution time for mesh.update() = "
        << runTime.elapsedCpuTime() - timeBeforeMeshUpdate
        << " s" << endl;
        }
        //AMR
        ...//begin solving
    }
    }

```

Listing 2: AMR implementation in the Solver

Flame inversion and the formation of a tulip flame has been captured so far with the incipient development of asymmetries in one of the flame lobes propagating along the channel's corners. The results so far are encouraging but a detailed analysis of mesh-induced instabilities to the flame morphology needs being done before using AMR confidently. Below are the first images (fig. 4.18) obtained from the simulation, which is still in progress, showing the structure of the flame in 3D at different stages (with U magnitude to observe the acceleration), and the mesh refinement at the flame front shown through a section cut along the x-y plane at the center of the channel.

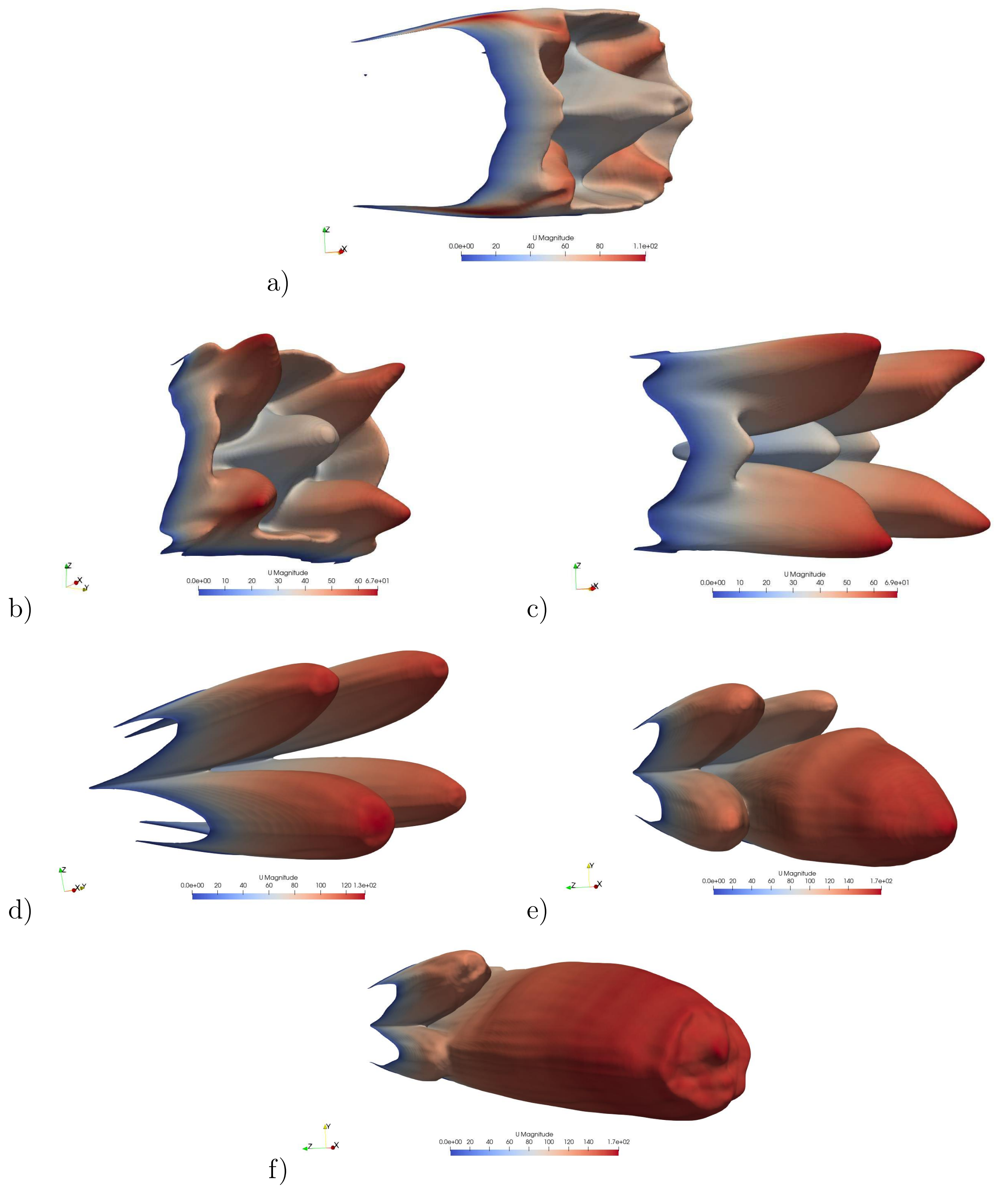

Figure 4.18: FA with AMR 3D channel: a) Initial ignition of the flame at $t = 2 \times 10^{-4}$ s; b) the flame starts to evolve in a characteristic "tulip shape", $t = 3 \times 10^{-4}$ s; c) the "tulip shape" come out developing four "lobes", $t = 7 \times 10^{-4}$ s; d) the bottom right corner lobe begins getting bigger, $t = 9.5 \times 10^{-4}$ s; e) the bigger lobe is getting bigger and embedding the other lobes, $t = 1.12 \times 10^{-3}$ s f) the flame seems develop a "finger shape" accelerating, $t = 1.39 \times 10^{-3}$ s

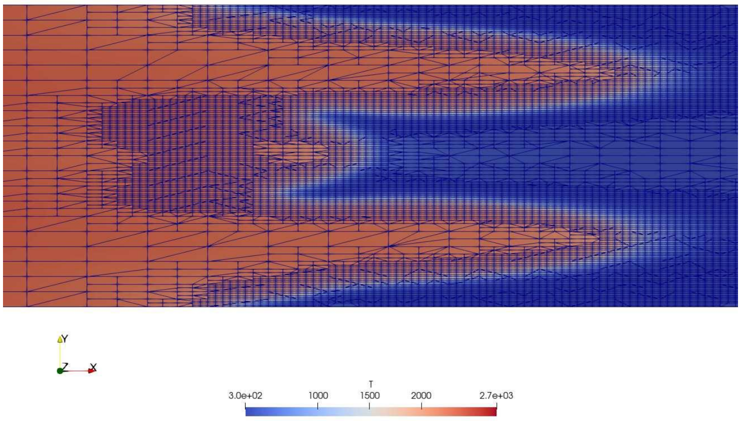

Figure 4.19: FA with AMR 3D channel clip, showing mesh refinement at step $t = 5 \times 10^{-4}$ s

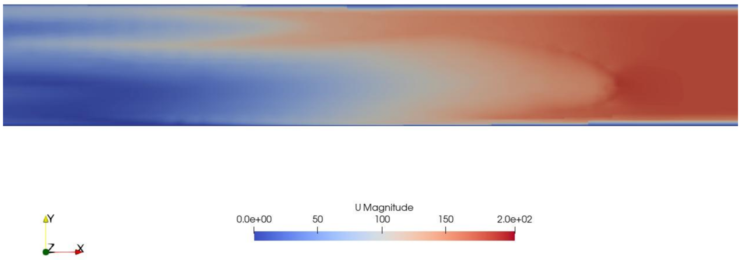

Figure 4.20: FA with AMR 3D channel clip, U magnitude field at the last step recorded of $t = 11.2 \times 10^{-3}$ s

Chapter 5

Conclusion and perspectives

- Numerical framework developed in Open Foam was tested to efficiently simulate flame acceleration and transition to detonation in obstructed and unobstructed channels. The experimentally observed regimes and trends were captured for increasing blockage ratio while keeping the initial pressure fixed, and for decreasing initial pressure while keeping the blockage ratio fixed. Specifically see table 5.1 and 5.2

BR	**Regime**
0.2	Steady state detonation
0.4	Sub-CJ detonation
0.6	Quasi-detonation

Table 5.1: Regimes observed at different blockage rations (BR) and initial pressure ($p_0 =$ 100kPa).

$\boldsymbol{p_0}$ **(kPa)**	**Regime**
100	Quasi-detonation
50	Quasi-detonation
25	Choked flame

Table 5.2: Regimes observed at different initial pressure p_0kPa at the same $BR = 0.6$.

- Numerical tests for unobstructed channels (1 mm in length) resulted in detonation onset as a result of viscous heating; x_{DDT} was observed to be dependent on the resolution used.

- Adaptive mesh refinement was implemented and currently being teste. The flame shape thus far seems to be reasonable and in agreement with the expected behavior.

- Before the end of my Internship we carried out new simulations using a different mesh domain, called "Orifice plate", in order to analyze the abrupt blockage ratio at different initial pressure ($p_0 = 25, 50, 100$ kPa) and compare it with the studies done in the paper of [3] . I plan to perform additional quantitative and complete analysis of results with the aim of having a first draft of a conference paper to be submitted to the 29th International Colloquium on the Dynamics of Explosion and Reactive Systems.
- High speed reacting flows and in particular DDT are cool!

Bibliography

[1] Henry G Weller, Gavin Tabor, Hrvoje Jasak, and Christer Fureby. A tensorial approach to computational continuum mechanics using object-oriented techniques. *Computers in physics*, 12(6):620–631, 1998.

[2] Alexander Kurganov, Sebastian Noelle, and Guergana Petrova. Semidiscrete central-upwind schemes for hyperbolic conservation laws and hamilton–jacobi equations. *SIAM Journal on Scientific Computing*, 23(3):707–740, 2001.

[3] G Ciccarelli and S Dorofeev. Flame acceleration and transition to detonation in ducts. *Progress in energy and combustion science*, 34(4):499–550, 2008.

[4] Elaine S Oran and Vadim N Gamezo. Origins of the deflagration-to-detonation transition in gas-phase combustion. *Combustion and flame*, 148(1-2):4–47, 2007.

[5] Ashley M Coates, Donovan L Mathias, and Brian J Cantwell. Numerical investigation of the effect of obstacle shape on deflagration to detonation transition in a hydrogen–air mixture. *Combustion and Flame*, 209:278–290, 2019.

[6] MF Ivanov, AD Kiverin, IS Yakovenko, and Michael A Liberman. Hydrogen–oxygen flame acceleration and deflagration-to-detonation transition in three-dimensional rectangular channels with no-slip walls. *International journal of hydrogen energy*, 38(36):16427–16440, 2013.

[7] Vadim N Gamezo, Christian L Bachman, and Elaine S Oran. Flame acceleration and ddt in large-scale obstructed channels filled with methane-air mixtures. *Proceedings of the Combustion Institute*, 38(3):3521–3528, 2021.

[8] MF Ivanov, AD Kiverin, MA Liberman, and VE Fortov. The flame-acceleration mechanism and transition to detonation of a hydrogen-oxygen mixture in a channel. In *Doklady Physics*, volume 55, pages 480–484. Springer, 2010.

[9] MF Ivanov, AD Kiverin, and Michael A Liberman. Flame acceleration and ddt of hydrogen–oxygen gaseous mixtures in channels with no-slip walls. *International journal of hydrogen energy*, 36(13):7714–7727, 2011.

[10] Michael A Liberman, AD Kiverin, and MF Ivanov. Regimes of chemical reaction waves initiated by nonuniform initial conditions for detailed chemical reaction models. *Physical review E*, 85(5):056312, 2012.

[11] Alexey D Kiverin, David R Kassoy, Mikhail F Ivanov, and Michael A Liberman. Mechanisms of ignition by transient energy deposition: Regimes of combustion wave propagation. *Physical Review E*, 87(3):033015, 2013.

[12] AD Kiverin, IS Yakovenko, and MF Ivanov. On the structure and stability of supersonic hydrogen flames in channels. *International Journal of Hydrogen Energy*, 41(47):22465–22478, 2016.

[13] Alexey D Kiverin and Ivan S Yakovenko. Regimes of high-speed hydrogen flame propagation in channels: classification and criteria of realization. *Combustion Science and Technology*, 192(1):112–129, 2020.

[14] Aleksei Dmitrievich Kiverin and Ivan Sergeevich Yakovenko. High-speed flame propagation in a channel and transition to detonation. *High Temperature*, 58(4):647–654, 2020.

[15] AD Kiverin, AE Smygalina, and IS Yakovenko. The classification of the scenarios of fast combustion wave development and deflagration-to-detonation transition in channels. *Russian Journal of Physical Chemistry B*, 14(4):607–613, 2020.

[16] Damir M Valiev, Vitaly Bychkov, V'yacheslav Akkerman, and Lars-Erik Eriksson. Different stages of flame acceleration from slow burning to chapman-jouguet deflagration. *Physical Review E*, 80(3):036317, 2009.

[17] RS Chue, JF Clarke, and JH Lee. Chapman-jouguet deflagrations. *Proceedings of the Royal Society of London. Series A: Mathematical and Physical Sciences*, 441(1913):607–623, 1993.

[18] DM Valiev, Vitaly Bychkov, Vyacheslav Akkerman, L-E Eriksson, and Chung K Law. Quasi-steady stages in the process of premixed flame acceleration in narrow channels. *Physics of Fluids*, 25(9):096101, 2013.

[19] I Brailovskya and G Sivashinsky. Hydraulic resistance and multiplicity of detonation regimes. *Combustion and flame*, 122(1-2):130–138, 2000.

[20] I Brailovsky, L Kagan, and G Sivashinsky. Combustion waves in hydraulically resisted systems. *Philosophical Transactions of the Royal Society A: Mathematical, Physical and Engineering Sciences*, 370(1960):625–646, 2012.

[21] L Kagan, P Gordon, and G Sivashinsky. An asymptotic study of the transition from slow to fast burning in narrow channels. *Proceedings of the Combustion Institute*, 35(1):913–920, 2015.

[22] Leonid Kagan and Gregory Sivashinsky. Parametric transition from deflagration to detonation: Runaway of fast flames. *Proceedings of the Combustion Institute*, 36(2):2709–2715, 2017.

[23] B Deshaies and G Joulin. Flame-speed sensitivity to temperature changes and the deflagration-to-detonation transition. *Combustion and flame*, 77(2):201–212, 1989.

[24] V'yacheslav Akkerman, Vitaly Bychkov, Mikhail Kuznetsov, Chung K Law, Damir Valiev, and Ming-Hsun Wu. Fast flame acceleration and deflagration-to-detonation transition in smooth and obstructed tubes, channels and slits. In *8th US National Combustion Meeting 2013*, volume 2, pages 970–978. Western States Section/Combustion Institute, 2013.

[25] BA V'yacheslav Slava. Modeling and simulation of turbulent combustion 569-583, 2018.

[26] Mohammed Alkhabbaz, Olatunde Abidakun, Damir Valiev, and V'yacheslav Akkerman. Impact of the lewis number on finger flame acceleration at the early stage of burning in channels and tubes. *Physics of Fluids*, 31(8):083606, 2019.

[27] Edyta Dziemińska and A Koichi Hayashi. Auto-ignition and ddt driven by shock wave–boundary layer interaction in oxyhydrogen mixture. *International Journal of hydrogen energy*, 38(10):4185–4193, 2013.

[28] Motoki Fukuda, Edyta Dzieminska, A Koichi Hayashi, Eisuke Yamada, and Nobuyuki Tsuboi. Effect of wall conditions on ddt in hydrogen–oxygen mixtures. *Shock Waves*, 23(3):191–200, 2013.

[29] Takuya Machida, Makoto Asahara, A Koichi Hayashi, and Nobuyuki Tsuboi. Three-dimensional simulation of deflagration-to-detonation transition with a detailed chemical reaction model. *Combustion Science and Technology*, 186(10-11):1758–1773, 2014.

[30] PA Urtiew and AK Oppenheim. Experimental observations of the transition to detonation in an explosive gas. *Proceedings of the Royal Society of London. Series A. Mathematical and Physical Sciences*, 295(1440):13–28, 1966.

[31] J Melguizo-Gavilanes and R Houim. Experimental and numerical study of flame acceleration and transition to detonation in narrow channels. In *US National Combustion Meeting, College Park, MD*, page 40, 2017.

[32] Wenhu Han, Yang Gao, and Chung K Law. Flame acceleration and deflagration-to-detonation transition in micro-and macro-channels: An integrated mechanistic study. *Combustion and Flame*, 176:285–298, 2017.

[33] Cheng Wang, Yongyao Zhao, and Bo Zhang. Numerical simulation of flame acceleration and deflagration-to-detonation transition of ethylene in channels. *Journal of Loss Prevention in the Process Industries*, 43:120–126, 2016.

[34] Feichi Zhang, Henning Bonart, Thorsten Zirwes, Peter Habisreuther, Henning Bockhorn, and Nikolaos Zarzalis. Direct numerical simulation of chemically reacting flows with the public domain code openfoam. In *High Performance Computing in Science and Engineering '14*, pages 221–236. Springer, 2015.

[35] Jin Huang, Wenhu Han, Xiangyu Gao, and Cheng Wang. Effects of heat loss and viscosity friction at walls on flame acceleration and deflagration to detonation transition. *Chinese Physics B*, 28(7):074704, 2019.

[36] Huahua Xiao, Qingsong Wang, Xuechao He, Jinhua Sun, and Xiaobo Shen. Experimental study on the behaviors and shape changes of premixed hydrogen–air flames propagating in horizontal duct. *International journal of hydrogen energy*, 36(10):6325–6336, 2011.

[37] Huahua Xiao, Qingsong Wang, Xiaobo Shen, Weiguang An, Qiangling Duan, and Jinhua Sun. An experimental study of premixed hydrogen/air flame propagation in a partially open duct. *International Journal of Hydrogen Energy*, 39(11):6233–6241, 2014.

[38] Huahua Xiao, Ryan W Houim, and Elaine S Oran. Formation and evolution of distorted tulip flames. *Combustion and Flame*, 162(11):4084–4101, 2015.

[39] Huahua Xiao, Qiangling Duan, and Jinhua Sun. Premixed flame propagation in hydrogen explosions. *Renewable and Sustainable Energy Reviews*, 81:1988–2001, 2018.

[40] Minggao Yu, Kai Zheng, Ligang Zheng, Tingxiang Chu, and Pinkun Guo. Scale effects on premixed flame propagation of hydrogen/methane deflagration. *international journal of hydrogen energy*, 40(38):13121–13133, 2015.

[41] Ming-hsun Wu, MP Burke, S Ff Son, and RA Yetter. Flame acceleration and the transition to detonation of stoichiometric ethylene/oxygen in microscale tubes. *Proceedings of the Combustion Institute*, 31(2):2429–2436, 2007.

[42] Ming-Hsun Wu and Chan-Yu Wang. Reaction propagation modes in millimeter-scale tubes for ethylene/oxygen mixtures. *Proceedings of the Combustion Institute*, 33(2):2287–2293, 2011.

[43] HP Chan and MH Wu. Stages of flame acceleration and detonation transition in a thin channel filled with stoichiometric ethylene/oxygen mixture. In *26th International Colloquium on the Dynamics of Explosions and Reactive Systems, Boston, MA*, page 6, 2017.

[44] Hao-Wei Ssu and Ming-Hsun Wu. Formation and characteristics of composite reaction–shock clusters in narrow channels. *Proceedings of the Combustion Institute*, 38(3):3473–3480, 2021.

[45] Cheng Wang, Shuanghe Wu, Yongyao Zhao, and Emmanuel Kwasi Addai. Experimental investigation on explosion flame propagation of h2-o2 in a small scale pipeline. *Journal of Loss Prevention in the Process Industries*, 49:612–619, 2017.

[46] Robert Blanchard, Detlef Arndt, Rainer Grätz, and Swen Scheider. Effect of ignition position on the run-up distance to ddt for hydrogen–air explosions. *Journal of loss prevention in the process industries*, 24(2):194–199, 2011.

[47] Christophe Proust. Gas flame acceleration in long ducts. *Journal of Loss Prevention in the Process Industries*, 36:387–393, 2015.

[48] S Kerampran, D Desbordes, and B Veyssiere. Study of the mechanisms of flame acceleration in a tube of constant cross section. *Combustion science and technology*, 158(1):71–91, 2000.

[49] S Kerampran, D Desbordes, B Veyssière, and Lux Bauwens. Flame propagation in a tube from closed to open end. In *39th Aerospace Sciences Meeting and Exhibit*, page 1082, 2001.

[50] Geraint Thomas, Gwyn Oakley, and Richard Bambrey. An experimental study of flame acceleration and deflagration to detonation transition in representative process piping. *Process Safety and Environmental Protection*, 88(2):75–90, 2010.

[51] Shinichi Maeda, Masashi Fujisawa, Shogo Ienaga, Keisuke Hirahara, and Tetsuro Obara. Effect of sandpaper-like small wall roughness on deflagration-to-detonation transition in a hydrogen–oxygen mixture. *Proceedings of the Combustion Institute*, 37(3):3609–3616, 2019.

[52] Keisuke Aizawa, Satoru Yoshino, Toshio Mogi, Hiroumi Shiina, Yuji Ogata, Yuji Wada, and A Koichi Hayashi. Study of detonation initiation in hydrogen/air flow. *Shock Waves*, 18(4):299–305, 2008.

[53] M Kuznetsov, V Alekseev, I Matsukov, and SJSW Dorofeev. Ddt in a smooth tube filled with a hydrogen–oxygen mixture. *Shock waves*, 14(3):205–215, 2005.

[54] M Kuznetsov, M Liberman, and I Matsukov. Experimental study of the preheat zone formation and deflagration to detonation transition. *Combustion science and technology*, 182(11-12):1628–1644, 2010.

[55] JW Meyer, PA Urtiew, and AK Oppenheim. On the inadequacy of gasdynamic processes for triggering the transition to detonation. *Combustion and Flame*, 14(1):13–20, 1970.

[56] MA Liberman, MF Ivanov, AD Kiverin, MS Kuznetsov, TV Rakhimova, and AA Chukalovskii. On the mechanism of the deflagration-to-detonation transition in a hydrogen-oxygen mixture. *Journal of Experimental and Theoretical Physics*, 111(4):684–698, 2010.

[57] Jorge Yanez and Mike Kuznetsov. Experimental study and theoretical analysis of a 'strange wave'. *Combustion and Flame*, 167:494–496, 2016.

[58] YA Baranyshyn, PN Krivosheyev, OG Penyazkov, and KL Sevrouk. Flame front dynamics studies at deflagration-to-detonation transition in a cylindrical tube at low-energy initiation mode. *Shock Waves*, 30(3):305–313, 2020.

[59] Pavel Krivosheyev, Oleg Penyazkov, and Aliaksei Sakalou. Analysis of the final stage of flame acceleration and the onset of detonation in a cylindrical tube using high-speed stereoscopic imaging. *Combustion and Flame*, 216:146–160, 2020.

[60] M Kuznetsov, V Alekseev, A Bezmelnitsyn, W Breitung, SB Dorofeev, I Matsukov, A Veser, and Yu Yankin. *Effect of obstacle geometry on behaviour of turbulent flames.* Forschunszentrum Karlsruhe, 1999.

[61] Andrzej Teodorczyk, P Drobniak, and A Dabkowski. Fast turbulent deflagration and ddt of hydrogen–air mixtures in small obstructed channel. *International Journal of Hydrogen Energy*, 34(14):5887–5893, 2009.

[62] Vadim N Gamezo, Takanobu Ogawa, and Elaine S Oran. Numerical simulations of flame propagation and ddt in obstructed channels filled with hydrogen–air mixture. *Proceedings of the Combustion Institute*, 31(2):2463–2471, 2007.

[63] Francisco X Romo. Design and optimization of a deflagration to detonation transition (ddt) section. 2012.

[64] Andre Vagner Gaathaug, Knut Vaagsaether, and Dag Bjerketvedt. Experimental and numerical investigation of ddt in hydrogen–air behind a single obstacle. *International Journal of Hydrogen Energy*, 37(22):17606–17615, 2012.

[65] Kirk A Strebel. Simulations of thermophoretic deposition in wavy channels. 2010.

[66] Zakaria Mansouri. Combustion in wavy micro-channels for thermo-photovoltaic applications–part i: Effects of wavy wall geometry, wall temperature profile and reaction mechanism. *Energy conversion and management*, 198:111155, 2019.

[67] Reza Soleimanpour and Hossain Nemati. Numerical investigation of deflagration to detonation transition in closed ducts under various working conditions. *Acta Astronautica*, 162:109–120, 2019.

[68] Alexander Burcat and Branko Ruscic. Third millenium ideal gas and condensed phase thermochemical database for combustion (with update from active thermochemical tables). Technical report, Argonne National Lab.(ANL), Argonne, IL (United States), 2005.

[69] William Sutherland. Lii. the viscosity of gases and molecular force. *The London, Edinburgh, and Dublin Philosophical Magazine and Journal of Science*, 36(223):507–531, 1893.

[70] Bruce E Poling, John M Prausnitz, and John P O'connell. *Properties of gases and liquids*. McGraw-Hill Education, 2001.

[71] Thierry Poinsot and Denis Veynante. *Theoretical and numerical combustion*. RT Edwards, Inc., 2005.

[72] Mitchell D Smooke. The computation of laminar flames. *Proceedings of the Combustion Institute*, 34(1):65–98, 2013.

[73] R Mével, S Javoy, F Lafosse, N Chaumeix, G Dupré, and C-E Paillard. Hydrogen–nitrous oxide delay times: Shock tube experimental study and kinetic modelling. *Proceedings of The Combustion Institute*, 32(1):359–366, 2009.

[74] RP Lindstedt and HJ Michels. Deflagration to detonation transitions and strong deflagrations in alkane and alkene air mixtures. *Combustion and Flame*, 76(2):169–181, 1989.

[75] M Kuznetsov, RK Singh, W Breitung, G Stern, J Grune, A Friedrich, K Sempert, and A Veser. Evaluation of structural integrity of typical dn15 tubes under detonation loads. *Report Forschungszentrum Karlsruhe*, 2003.

[76] Joseph E Shepherd. Detonation in gases. *Proceedings of the Combustion Institute*, 32(1):83–98, 2009.

[77] CM Romick, TD Aslam, and JM Powers. The effect of diffusion on the dynamics of unsteady detonations. *Journal of Fluid Mechanics*, 699:453–464, 2012.

[78] David C Arney and Joseph E Flaherty. An adaptive local mesh refinement method for time-dependent partial differential equations. *Applied numerical mathematics*, 5(4):257–274, 1989.

[79] Ahmad Baniabedalruhman. Dynamic meshing around fluid-fluid interfaces with applications to droplet tracking in contraction geometries. 2015.